Supporting Information

Solvent- and Anion-induced Interconversions of Metal-Organic Cages

Yu-Hao Li,[†] Ji-Jun Jiang,[†] Yan-Zhong Fan,[†] Zhang-Wen Wei,[†] Cheng-Xia Chen,[†] Hui-Juan Yu,[†] Shao-Ping Zheng,[†] Dieter Fenske,[†] Cheng-Yong Su[†,*] and Mihail Barboiu[†,‡,*]

[†]MOE Laboratory of Bioinorganic and Synthetic Chemistry, Lehn Institute of Functional materials, School of Chemistry and Chemical Engineering, Sun Ya t-Sen University, Guangzhou 510275, China.
[‡]Adaptive Supramolecular Nanosystems Group, Institut Europeen des Membranes, University of Montpellier ENSCM-UMR CNRS 5635, Place Eugene Bataillon CC047, Montpellier, F-34095, France

Contents

1. General Method

All chemicals were of reagent grade obtained from commercial sources and used without further purification. ^{1}H NMR, ^{19}F NMR spectra was recorded on Bruker AVANCE III 400 (400 MHz). HRESI-TOF mass spectra were measured on Bruker maXis 4G. The data analyses of ESI-TOF mass spectra were processed on Bruker Data Analysis. Reflection intensity data were collected at 150 K on an Agilent Sapphire3 Gemini Ultra single crystal diffractometer using Cu radiation (40 kV, 40 mA, λ = 1.54178 Å). The elemental analyses were performed with Vario EL cube elemental analyzer. IR spectra were measured as KBr pellets using a Nicolet/Nexus-670 FTIR spectrometer.

2. Synthesis and Characterization

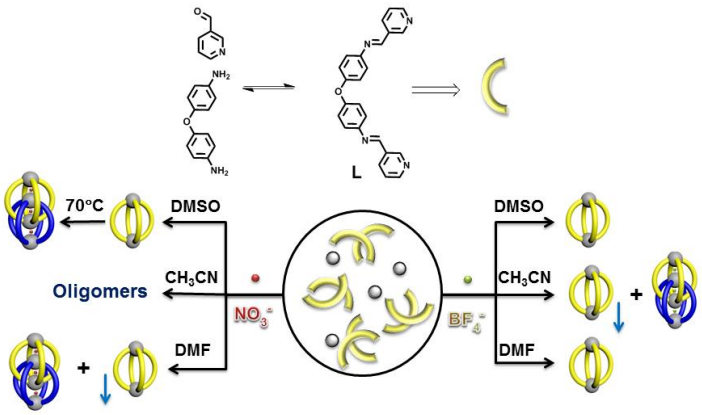

Scheme S1. Syntheses and separation of monomeric and dimeric cages in different solvents by using ligand L and $Pd(BF_4)_2$ or $Pd(NO_3)_2$.

2.1 Synthesis of the ligand L

The ligand N,N'-(oxybis(4,1-phenylene))bis(1-(pyridin-3-yl)- methanimine) (**L**) was prepared according to an adapted literature procedure.[1] 4,4'-Oxydianiline (260 mg, 1.3 mmol) and 3-pyridinecarboxaldehyde (267 µL, 2.8 mmol) were mixed in 8 mL ethanol, and a catalytic amount of *p*-toluenesulfonic acid was added to the mixture. The resulting mixture was stirred for 3 hours at room temperature, during which the yellowish solid precipitates from the solution. The precipitate was isolated by filtration, washed with cold ethanol and dried under reduced pressure to afford the desired product **L** as a yellowish solid (330 mg, 67%). ^{1}H NMR (400MHz, DMSO-d_6, 298 K): δ9.07 (d, J = 1.5 Hz, 2H), 8.77 (s, 2H), 8.72 (dd, J = 4.8, 1.7 Hz, 2H), 8.33 (dt, J = 8.0, 1.9 Hz, 2H), 7.57 (dd, J = 7.9, 4.8 Hz, 2H), 7.45-7.37 (m, 4H), 7.17-7.09 (m, 4H).

2.2 Synthesis of the cages [MOC-20](BF$_4$)$_4$ and [3BF$_4$@MOC-21](BF$_4$)$_5$

Subcomponent self-assembly: 3-Formylpyridine (45.8 mg, 427 µmol), 4,4′-oxydianiline (42.8 mg, 213 µmol) and tetrakis(acetonitrile)palladium(II) tetrafluoroborate (47.5 mg, 107 µmol) were dissolved in acetonitrile (10 mL). The resulting yellow solution was stirred at 50 °C overnight, after which yellow precipitates formed. The mixtures were centrifuged, of which the

supernate was transferred to another centrifuge tube. The precipitate was washed successively with acetonitrile and diethyl ether, and dried to afford the monomeric cage **[MOC-20]·4BF$_4$** (Yield 40% based on metal). The product in supernate was precipitated as yellow powder to give the dimeric cage **[3BF$_4^-$@MOC-21]·5BF$_4$** by addtion of diethyl ether (Yield 42% based on metal). For monomeric cage **[MOC-20](BF$_4$)$_4$**: ^{1}H NMR (400 MHz, DMSO-d_6, 298 K), δ 10.17 (s, 8H), 9.44 (d, J = 5.7 Hz, 8H), 8.69 (s, 8H), 8.42 (d, J = 8.0 Hz, 8H), 7.89 (dd, J = 7.7, 6.0 Hz, 9H), 7.37 (d, J = 8.7 Hz, 16H), 7.04 (d, J = 8.7 Hz, 16H). HRESI-MS, *m/z* $[C_{96}H_{72}N_{16}O_4Pd_2]^{4+}$ calcd (found): 431.6012 (431.5964). IR (KBr, cm^{-1}), ν 3436, 3090, 1630, 1581, 1493, 1435, 1328, 1237, 1196, 1158, 1073, 835, 698, 525, 475. Elemental analysis ($C_{192}H_{144}B_8F_{32}N_{32}O_8Pd_4\cdot 10H_2O$) calcd (%) : C 53.29, H 3.82, N 10.36; found(%): C 53.02, H 3.637, N 10.11. For dimeric cage **[3BF$_4$@MOC-21](BF$_4$)$_5$**: ^{1}H NMR (400 MHz, CD_3CN, 298 K), δ 10.41 (s, 8H), 10.34 (s, 8H), 9.46 (d, J = 5.6 Hz, 8H), 9.31 (d, J = 5.4 Hz, 8H), 8.85 (s, 8H), 8.53 (d, J = 7.9 Hz, 8H), 8.15 (d, J = 7.9 Hz, 8H), 8.12 (s, 8H), 7.86 (dd, J = 7.7, 6.0 Hz, 8H), 7.30 (d, J = 8.5 Hz, 16H), 7.26 (dd, J = 7.6, 6.1 Hz, 8H), 6.77 (d, J = 8.6 Hz, 16H), 6.47 (d, J = 8.5 Hz, 16H), 5.69 (d, J = 8.6 Hz, 16H). ^{19}F NMR (377 MHz, CD_3CN, 298 K) δ -139.58, -140.25, -151.56. HRESI-MS, *m/z* $[C_{192}H_{144}N_{32}O_8Pd_4\cdot(BF_4)_3]^{5+}$ calcd (found): 742.5631 (742.5663). IR (KBr, cm^{-1}), ν 3435, 3094, 1630, 1581, 1493, 1435, 1375, 1328, 1237, 1196, 1159, 1073, 871, 835, 697, 553, 473.

One pot reaction of 3-formylpyridine, 4,4′-oxydianiline and $Pd(BF_4)_2$ in DMF resulted a light yellow clear solution, from which the precipitation was obtained by adding diethyl ether. The yellow precipitating powder is proved to be the monomeric cage **[MOC-20](BF$_4$)$_4$** by ^{1}H NMR measurement. Elemental analysis for **[MOC-20](BF$_4$)$_4$** ($C_{96}H_{72}B_4F_{16}N_{16}O_4Pd_2\cdot 2DMF\cdot 7H_2O$) calcd (%): C 52.22, H 4.30, N 10.75; found: C 52.18, H 3.956, N 10.45.

Direct self-assembly: The ligand **L** *(*50 *mg*, 132 μmol*)*, tetrakis(acetonitrile)palladium(II) tetrafluoroborate (29.6 *mg*, 67 μmol*)* was dissolved in 10 mL CH_3CN. The resulting yellow solution became turbid after 3 minutes. After stirring at 50 °C for another 4 hours, the mixtures were centrifuged, of which supernate was transferred to another centrifuge tube. The precipitate was washed successively with acetonitrile and diethyl ether, and then dried under reduced pressure to give monomeric cage **[MOC-20](BF$_4$)$_4$** as yellow solid (47%). Product in supernate was precipitated as yellow powder to give dimeric cage **[3BF$_4$@MOC-21](BF$_4$)$_5$** by addition of diethyl ether (40%).

2.3 Synthesis of the cages [MOC-20](NO$_3$)$_4$ and [3NO$_3$@MOC-21](NO$_3$)$_5$

Subcomponent self-assembly: The monomeric cage **[MOC-20](NO$_3$)$_4$** and dimeric cage **[3NO$_3$@MOC-21](NO$_3$)$_5$** could also be synthesized from an one pot reaction containing a 4:2:1 mixture of subcomponents 3-formylpyridine, 4,4′-oxydianiline and $Pd(NO_3)_2$ in DMF at 50 °C. The main product is the dimeric cage **[3NO$_3$@MOC-21](NO$_3$)$_5$** isolated from the supernate

with a yield of 80%, while only a slight amount of precipitate product of the monomeric cage **[MOC-20](NO$_3$)$_4$** is obtained under this circumstance.

Direct self-assembly: The ligand **L** (31 mg, 82 μmol), Pd(NO$_3$)$_2$ (10.9 mg, 47 μmol) was dissolved in 5 mL DMF. The resulting yellow solution was stirred at 50 °C for 3 hours, after which yellow precipitates formed. The mixtures were centrifuged, of which supernate was transferred to another centrifuge tube. The precipitate was washed successively with DMF and diethyl ether, and then dried under reduced pressure to give monomeric cage **[MOC-20](NO$_3$)$_4$** as yellow solid. Yield: 24.6 mg, 60%. The product of dimeric cage **[3NO$_3$@MOC-21](NO$_3$)$_5$** in supernate was precipitated as yellow powder after addition of diethyl ether. Yield: 13.2 mg, 32%. For the monomeric cage **[MOC-20](NO$_3$)$_4$**: ^{1}H NMR (400 MHz, DMSO-d_6, 298 K), δ 10.21 (s, 8H), 9.46 (d, J = 5.5 Hz, 8H), 8.70 (s, 8H), 8.43 (d, J = 8.1 Hz, 8H), 7.90 (dd, J = 7.7, 5.9 Hz, 8H), 7.39 (d, J = 8.7 Hz, 16H), 7.07 (d, J = 8.7 Hz, 16H). HRESI-MS, *m/z* [C$_{96}$H$_{72}$N$_{16}$O$_4$Pd$_2$]$^{4+}$ calcd (found): 431.6003 (431.5964). Elemental analysis (C$_{96}$H$_{72}$N$_{20}$O$_{16}$Pd$_2$·0.5DMF·8H$_2$O) calcd (%): C 54.33, H 4.28, N 13.32; found (%): C 54.01, H 4.189, N 12.98. IR (KBr, cm^{-1}), ν 3435, 1628, 1494, 1383, 1239, 1197, 1106, 838, 700. For the dimeric cage **[3NO$_3$@MOC-21](NO$_3$)$_5$**: ^{1}H NMR (400 MHz, DMSO-d_6, 298 K), δ 10.58 (s, 16H), 9.71 (d, J = 5.5 Hz, 8H), 9.58 (d, J = 5.4 Hz, 8H), 8.83 (s, 8H), 8.62 (d, J = 8.0 Hz, 8H), 8.27 (s, 16H), 8.08 – 8.01 (m, 8H), 7.60 – 7.53 (m, 1H), 7.25 (d, J = 8.4 Hz, 16H), 6.80 (d, J = 8.6 Hz, 16H), 6.47 (d, J = 8.4 Hz, 16H), 5.69 (d, J = 8.6 Hz, 16H). HRESI-MS, *m/z* [C$_{192}$H$_{144}$N$_{32}$O$_8$Pd$_4$·(NO$_3$)$_3$]$^{5+}$ calcd (found): 727.7536 (727.7556). Elemental analysis (C$_{192}$H$_{144}$N$_{40}$O$_{32}$Pd$_4$·DMF) calcd (%): C 58.23, H 3.78, N 14.28; found (%): C 59.08, H 4.238, N 14.37. IR (KBr, cm^{-1}), ν 3434, 3059, 1660, 1630, 1582, 1493, 1382, 1235, 1197, 1104, 834, 698, 552, 474.

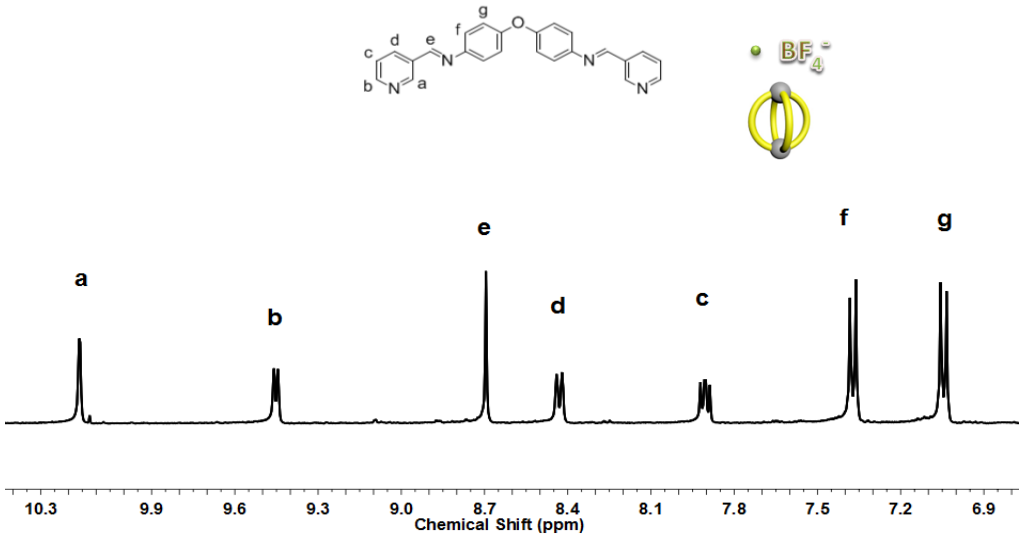

Figure S1. ^{1}H NMR spectrum of **[MOC-20](BF$_4$)$_4$** (400 MHz, DMSO-d_6, 298 K).

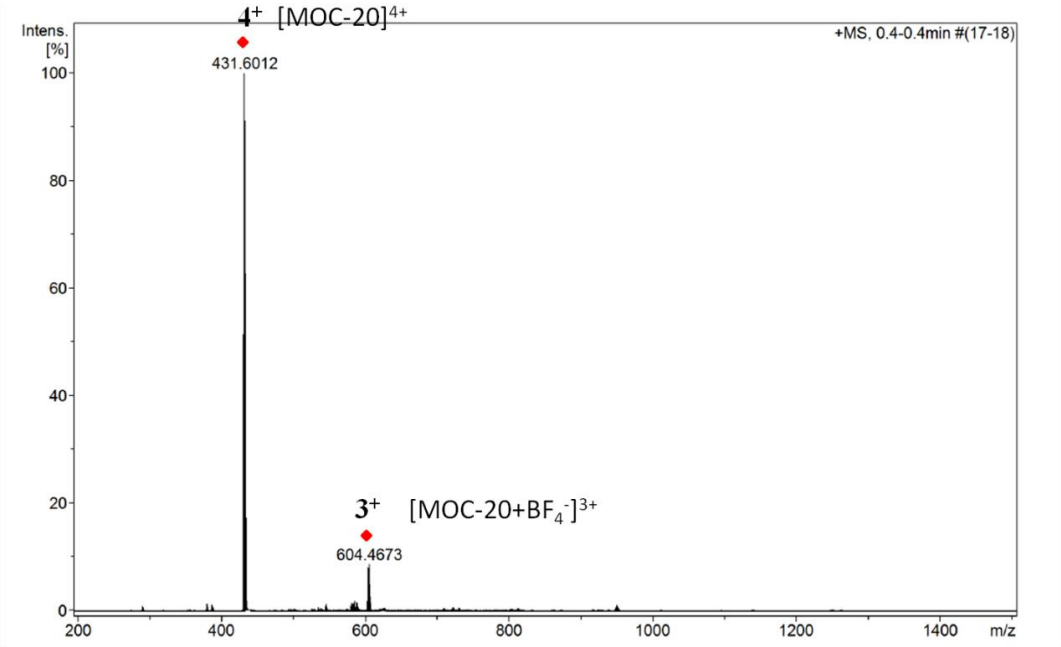

Figure S2. High resolution ESI-mass spectrum for **[MOC-20](BF$_4$)$_4$**

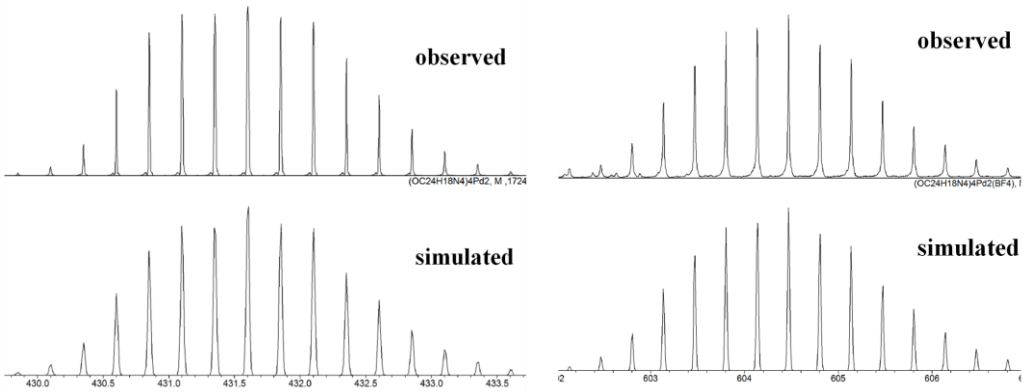

Figure S3. Isotopic distribution of peaks [**MOC-20**]$^{4+}$ and [**MOC-20**+**BF$_4$**]$^{3+}$.

Table S1. Selected mass information for 4^+ and 3^+ peaks of **MOC-20** (BF_4^- salt).

Selected mass information in the 4^+ peak						
Observed ion (m/z)	**Intensity**	**Resolution**	**FWHM**	**Theoretical mass**	**Difference (obs.–theo.)**	**Error (ppm)**
430.0990	184800	33816	0.0127	430.0999	-0.0009	-2.1
430.3486	631819	43654	0.0099	430.3500	-0.0014	-3.3
430.5992	1757152	52022	0.0083	430.5999	-0.0007	-1.6
430.8502	2904163	41723	0.0103	430.8501	0.0001	0.2
431.1008	3271533	30048	0.0143	431.1001	0.0007	1.6
431.3510	3280441	27976	0.0154	431.3503	0.0007	1.6
431.6012	3416616	24210	0.0178	431.6003	0.0009	2.1
431.8510	3211110	30863	0.0140	431.8506	0.0004	0.9

432.1008	3116324	34025	0.0127	432.1005	0.0003	0.7
432.3501	2390123	54460	0.0079	432.3508	-0.0007	-1.6
432.5998	1642820	53394	0.0081	432.6008	-0.0010	-2.3
432.8499	942509	47459	0.0091	432.8510	-0.0011	-2.5
433.1003	499909	41064	0.0105	433.1012	-0.0009	-2.1
433.3509	231359	33112	0.0131	433.3515	-0.0006	-1.4
433.6015	94969	28694	0.0151	433.6020	-0.0005	-1.2
Selected mass information in the 3^+ peak						
Observed ion (m/z)	**Intensity**	**Resolution**	**FWHM**	**Theoretical mass**	**Difference (obs.–theo.)**	**Error (ppm)**
602.4678	23329	25638	0.0235	602.4682	-0.0004	-0.7
602.8015	61826	30324	0.0199	602.8017	-0.0002	-0.3
603.1321	136506	32771	0.0184	603.1350	-0.0029	-4.8
603.4679	203512	36939	0.0163	603.4684	-0.0005	-0.8
603.8006	266021	41241	0.0146	603.8017	-0.0011	-1.8
604.1334	272176	39157	0.0154	604.1352	-0.0018	-3.0
604.4673	296646	40996	0.0147	604.4684	-0.0011	-1.8
604.8006	241410	38023	0.0159	604.8021	-0.0015	-2.5
605.1336	215425	38234	0.0158	605.1353	-0.0017	-2.8
605.4680	140045	33424	0.0181	605.4690	-0.0010	-1.7
605.8008	93307	31237	0.0194	605.8024	-0.0016	-2.6
606.1333	60004	32244	0.0188	606.1360	-0.0027	-4.5
606.4687	32688	28385	0.0214	606.4696	-0.0009	-1.5
606.8000	17603	25151	0.0241	606.8034	-0.0034	-5.6

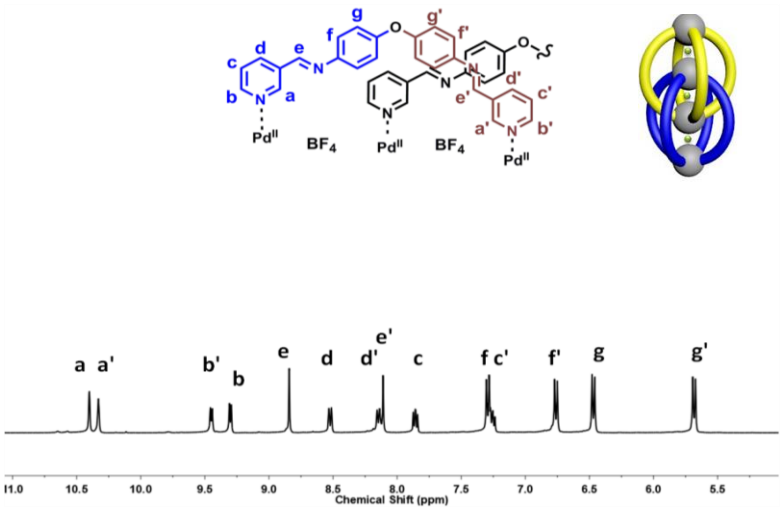

Figure S4. ^{1}H NMR spectrum of **[3BF_4@MOC-21](BF_4)$_5$**, assignment referring 2D spectra below (400 MHz, CD_3CN, 298 K).

The ^{19}F NMR spectrum of interlocked cage **[3BF_4@MOC-21](**BF_4**)$_5$** presents two peaks at -140.06 (central cavity) and -140.70 (two outer cavities) ppm respectively (Figure S5), corresponding to the encapsulated BF_4^- anions, while the peak observed at -151.60 ppm is corresponding to external free BF_4^-. The relatively broad peaks at -140.70 and -151.60 ppm are reminiscent with the exchange of BF_4^- between outer cavities of the interlocked cage and external solution, which is slow enough to be detected at NMR time scale.[2] On the contrary, the BF_4^- in the central pocket is closely locked and hardly exchanged.[3]

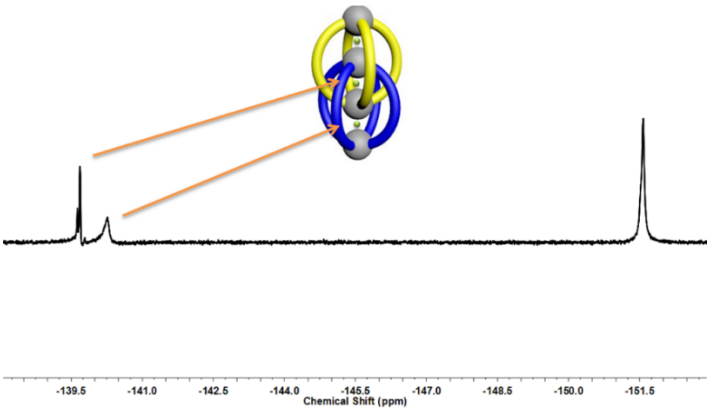

Figure S5. ^{19}F NMR spectrum of **[3BF_4@MOC-21](**BF_4**)$_5$** (376 MHz, CD_3CN, 298 K).

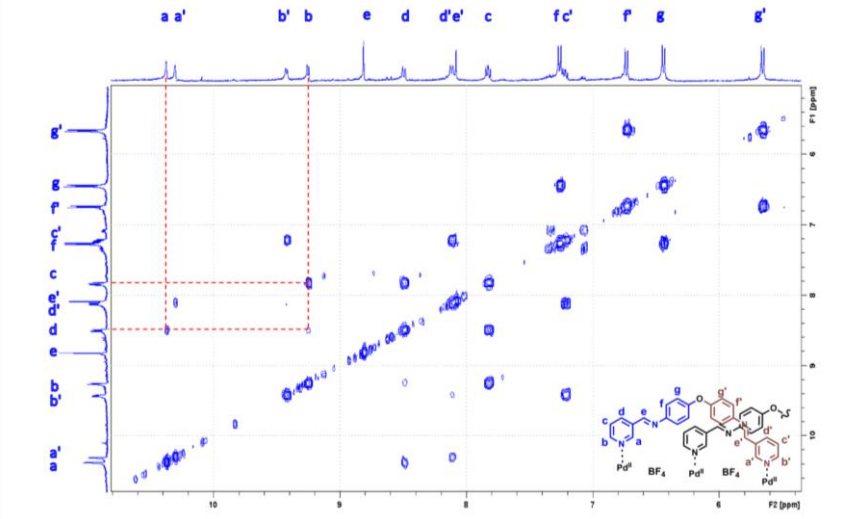

Figure S6. ^1H–^1H COSY spectrum of **[3BF_4@MOC-21](**BF_4**)$_5$** (400 MHz, CD_3CN, 298 K), peaks linked by red lines are from the same ligand.

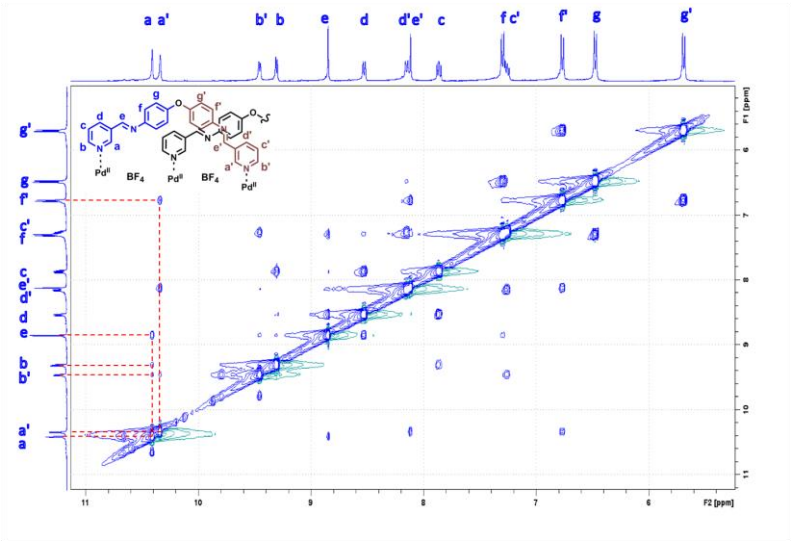

Figure S7. $^{1}H–^{1}H$ NOESY spectrum of **[3BF$_4$@MOC-21](BF$_4$)$_5$** (400 MHz, CD_3CN, 298 K). The proton H_a has cross peaks with both H_b and $H_{b'}$, therefore, we can attribute other peaks.

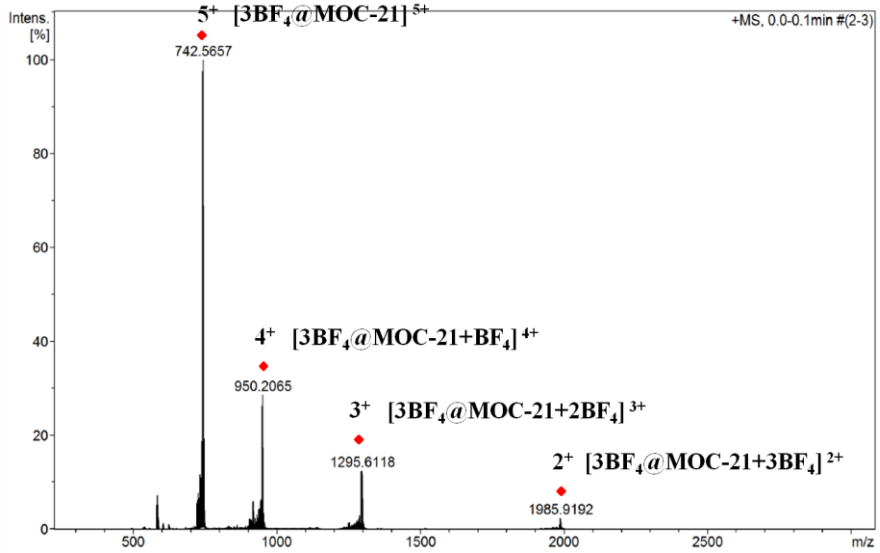

Figure S8. High resolution ESI-mass spectrum for **MOC-21** showing a family of peaks corresponding to {[**3BF$_4$@MOC-21](**BF$_4$)$_n$}$^{(5-n)+}$ (@ denotes encapsulation, n = 0-3) (Fig. S8

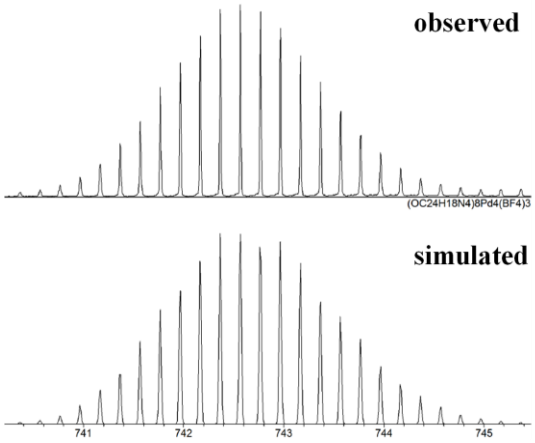

Figure S9. Observed and simulated isotopic patterns of 5^+ peak of **MOC-21**(BF_4^- salt).

Table S2. Selected mass information for 5^+ peaks of **MOC-21** (BF_4^- salt).

Selected mass information in the 5^+ peak						
Observed ion (m/z)	**Intensity**	**Resolution**	**FWHM**	**Theoretical mass**	**Difference (obs.–theo.)**	**Error (ppm)**
740.5650	29853	30356	0.0244	740.5631	0.0019	2.6
740.7645	47230	33307	0.0222	740.7630	0.0015	2.0
740.9651	78668	35635	0.0208	740.9629	0.0022	3.0
741.1648	129740	38303	0.0194	741.1629	0.0019	2.6
741.3653	209069	42852	0.0173	741.3629	0.0024	3.2
741.5653	297770	44767	0.0166	741.5629	0.0024	3.2
741.7654	427098	50493	0.0147	741.7630	0.0024	3.2
741.9655	523718	51598	0.0144	741.9630	0.0025	3.4
742.1655	627755	53850	0.0138	742.1631	0.0024	3.2
742.3656	732377	58516	0.0127	742.3631	0.0025	3.4
742.5657	750025	57905	0.0128	742.5631	0.0026	3.5
742.7657	720670	56934	0.0130	742.7631	0.0026	3.5
742.9658	659650	56317	0.0132	742.9631	0.0027	3.6
743.1658	552182	53329	0.0139	743.1632	0.0026	3.5
743.3657	447432	50404	0.0147	743.3633	0.0024	3.2
743.5657	334509	46560	0.0160	743.5634	0.0023	3.1
743.7659	241141	43905	0.0169	743.7635	0.0024	3.2
743.9658	175248	41246	0.0180	743.9637	0.0021	2.8
744.1660	114028	36259	0.0205	744.1638	0.0022	3.0
744.3657	74319	33890	0.0220	744.3639	0.0018	2.4
744.5663	51755	32777	0.0227	744.5640	0.0023	3.1
744.7664	38685	32146	0.0232	744.7642	0.0022	3.0
744.9662	31922	30184	0.0247	744.9643	0.0019	2.6

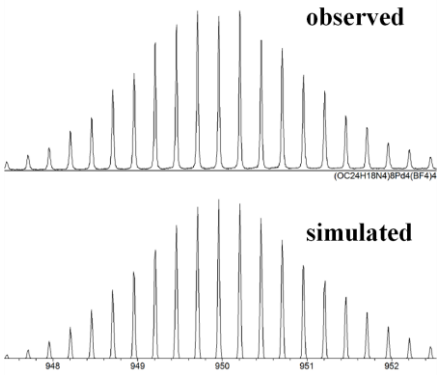

Figure S10. Observed and simulated isotope patterns of 4^+ peak of **MOC-21**(BF_4^- salt).

Table S3. Selected mass information for 4^+ peaks of **MOC-21** (BF_4^- salt).

Selected mass information in the 4^+ peak						
Observed ion (m/z)	**Intensity**	**Resolution**	**FWHM**	**Theoretical mass**	**Difference (obs.–theo.)**	**Error (ppm)**
947.7069	21280	31784	0.0298	947.7049	0.0020	2.1
947.9564	31409	34988	0.0271	947.9548	0.0016	1.7
948.2064	53816	37190	0.0255	948.2047	0.0017	1.8
948.4566	71327	36971	0.0257	948.4547	0.0019	2.0
948.7063	110028	39552	0.0240	948.7048	0.0015	1.6
948.9568	131217	39937	0.0238	948.9548	0.0020	2.1
949.2065	172887	42887	0.0221	949.2049	0.0016	1.7
949.4567	196864	45208	0.0210	949.4549	0.0018	1.9
949.7067	215410	44733	0.0212	949.7049	0.0018	1.9
949.9570	208711	44948	0.0211	949.9549	0.0021	2.2
950.2065	215561	45636	0.0208	950.2049	0.0016	1.7
950.4571	176156	42270	0.0225	950.4550	0.0021	2.2
950.7070	165080	42250	0.0225	950.7051	0.0019	2.0
950.9572	129262	42515	0.0224	950.9552	0.0020	2.1
951.2070	107920	38987	0.0244	951.2053	0.0017	1.8
951.4578	74111	35863	0.0265	951.4555	0.0023	2.4
951.7071	58412	33437	0.0285	951.7056	0.0015	1.6
951.9579	37902	34279	0.0278	951.9558	0.0021	2.2
952.2072	28406	33668	0.0283	952.2059	0.0013	1.4
952.4577	18284	31143	0.0306	952.4561	0.0016	1.7
952.7087	15463	28088	0.0339	952.7062	0.0025	2.6

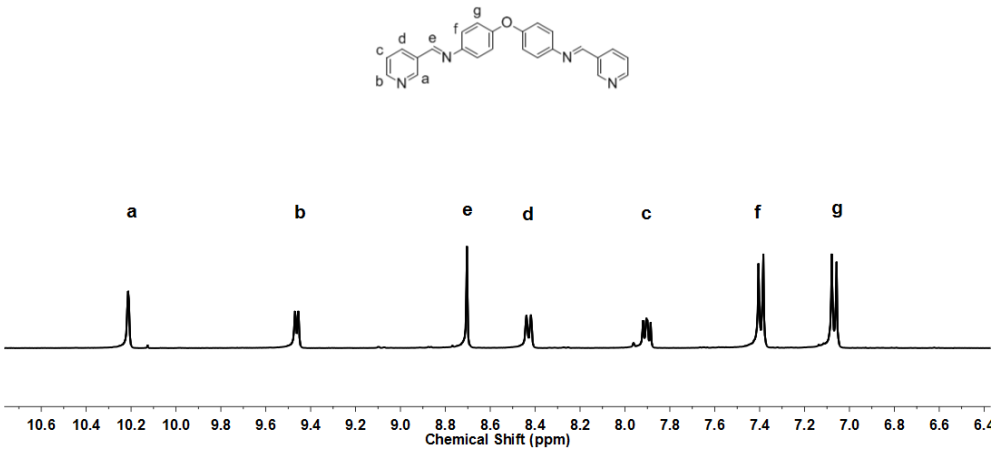

Figure S11. ^{1}H NMR spectrum of **[MOC-20](NO$_3$)$_4$** (400 MHz, DMSO-d_6, 298 K).

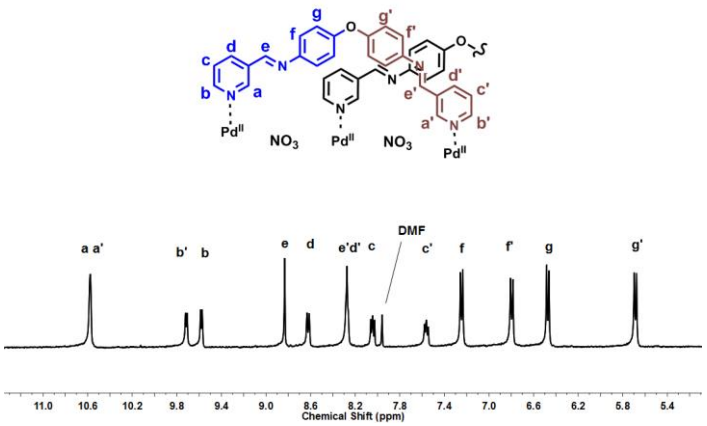

Figure S12. ^{1}H NMR spectrum of **[3NO$_3$@MOC-21](NO$_3$)$_5$** (400 MHz, DMSO-d_6, 298 K).

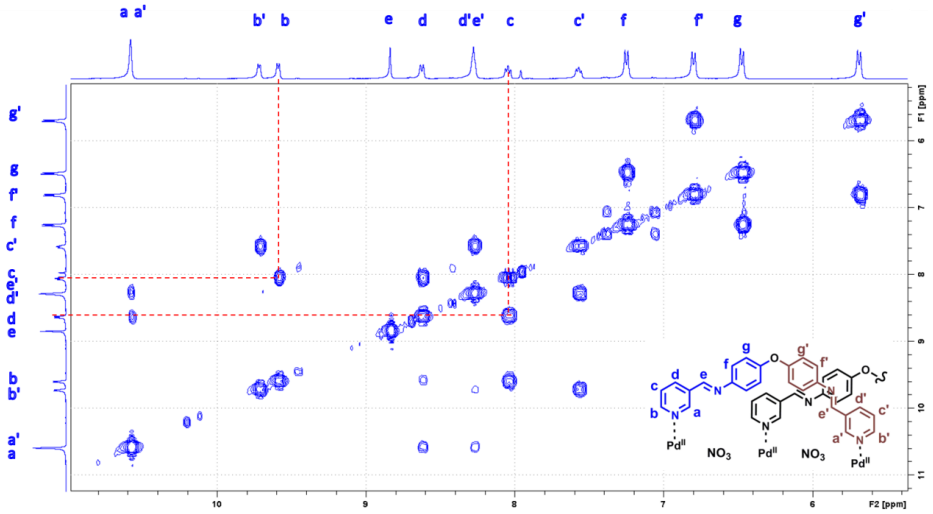

Figure S13. ^{1}H–^{1}H COSY spectrum of **[3NO$_3$@MOC-21](NO$_3$)$_5$** (400 MHz, DMSO-d_6, 298 K), peaks linked by red lines are from the same ligand.

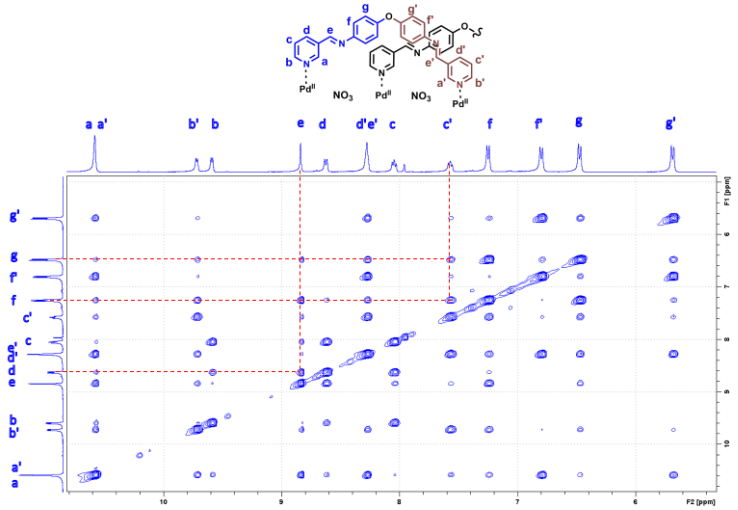

Figure S14. ^{1}H–^{1}H NOESY spectrum of **[3NO$_3$@MOC-21](NO$_3$)$_5$** (400 MHz, DMSO-d_6, 298 K). The triplet which have cross peaks with both H_f and H_g is $H_{c'}$, therefore we can attribute other peaks.

3. Crystallography

Crystals of the interlocked **[3BF_4@MOC-21](BF_4)$_5$** suitable for X-ray diffraction were obtained by slow diffusion of diisopropyl ether into an acetonitrile solution of complex **[3BF_4@MOC-21](BF_4)$_5$** in a few days. Crystals of **[2($I_{0.5}$+(BF_4)$_{0.5}$)+BF_4@MOC-21](BF_4)$_5$** suitable for X-ray diffraction were obtained by slow diffusion of diisopropyl ether into an acetonitrile solution of complex **[3BF_4@MOC-21](BF_4)$_5$** with the presence of two equivalent of tetrabutylammonium iodide in a few days.

The structure of **[3BF_4@MOC-21](BF_4)$_5$** was solved by direct methods and refined by full-matrix least squares against F^2 *of* all data using the SHELXTL program package. Anisotropical thermal factors were assigned to the non-hydrogen atoms. The positions of the hydrogen atoms were generated geometrically, assigned isotropic thermal parameters, and allowed to ride on their respective parent atoms before the final cycle of least-squares refinement. One BF_4^- anion is disordered over two positions and treated with part occupancy. All disordered solvent molecules are remove by SQUEEZE program. Geometric constraint was applied to one BF_4^- anion with SADI, ISOR and SIMU.

The structure of **[2($I_{0.5}$+(BF_4)$_{0.5}$)+BF_4@MOC-21](BF_4)$_5$** was solved by direct methods and refined by full-matrix least squares against F^2 *of* all data using the SHELXTL program package. Anisotropical thermal factors were assigned to the non-hydrogen atoms. BF_4^- guest anions in two outer cage cavities were partially replaced by I^- anions, and the fractional ratio between these two anions was freely refined as a result of about 50%. Some acetonitrile and BF_4^- molecules are disordered and refined with partial occupancy and restrains for idealized model. The positions of the hydrogen atoms were generated geometrically, assigned isotropic thermal parameters, and allowed to ride on their respective parent atoms before the final cycle of least-squares refinement.

Table S4. Crystal data and structure refinement for [**MOC-21** and **MOC-21-Cage-I**

Identification code	**[3BF_4@MOC-21](BF_4)$_5$**	**[2($I_{0.5}$+(BF_4)$_{0.5}$)+BF_4@MOC-21](BF_4)$_5$**
Empirical formula	$C_{98}H_{75}B_4F_{16}N_{17}O_4Pd_2$	$C_{106}H_{74.5}B_{3.5}F_{13.88}I_{0.5}N_{21}O_4Pd_2$
Formula weight	2114.79	2284.07
Temperature/K	173(2)	173(2)
Crystal system	monoclinic	monoclinic
Space group	*C*2/*c*	*C*2/*c*
a/Å	43.0462(13)	42.9184(7)
b/Å	20.7440(4)	20.7337(3)
c/Å	28.9748(7)	28.9827(4)
α/°	90	90
β/°	125.766(3)	125.0860(10)

γ/°	90	90
Volume/Å^3	20993.7(11)	21104.1(6)
Z	8	8
ρ_{calc}/g·cm^{-3}	1.338	1.438
μ/mm^{-1}	3.489	4.634
F(000)	8560.0	9203.0
Crystal size/mm^3	0.250 × 0.200 × 0.150	0.250 × 0.200 × 0.150
Radiation	Cu$K\alpha$ (λ = 1.54178)	Cu$K\alpha$ (λ = 1.54178)
2θ range for data collection/°	7.058 to 129.998	7.014 to 124.998
Index ranges	-50 ≤ h ≤ 32, -23 ≤ k ≤ 24, -26 ≤ l ≤ 34	-48 ≤ h ≤ 49, -23 ≤ k ≤ 17, -33 ≤ l ≤ 29
Reflections collected	35991	31255
Independent reflections	17774 [R_{int} = 0.0478, R_{sigma} = 0.0620]	16562 [R_{int} = 0.0401, R_{sigma} = 0.0489]
Data/restraints/parameters	17774/420/1293	16562/557/1475
Goodness-of-fit on F^2	1.045	1.033
Final R indexes [I>=2σ (I)]	R_1= 0.0927, wR_2= 0.2049	R_1= 0.0547, wR_2= 0.1468
Final R indexes [all data]	R_1= 0.1496, wR_2 = 0.2488	R_1= 0.0739, wR_2= 0.1640
Largest diff. peak/hole / e Å^{-3}	2.42/-1.59	1.16/-0.84

Table S5. Bond lengths and angles for **[3BF$_4$@MOC-21](BF$_4$)$_5$** and **[2(I$_{0.5}$+(BF$_4$)$_{0.5}$)+BF$_4$@MOC-21](BF$_4$)$_5$**

[3BF$_4$@MOC-21](BF$_4$)$_5$			**[2(I$_{0.5}$+(BF$_4$)$_{0.5}$)+BF$_4$@MOC-21](BF$_4$)$_5$**		
Atom	**Atom**	**Length/Å**	**Atom**	**Atom**	**Length/Å**
Pd1	N2	2.027(7)	Pd1	N2	2.031(4)
Pd1	N1	2.034(7)	Pd1	N1	2.032(4)
Pd1	N4	2.032(7)	Pd1	N4	2.033(4)
Pd1	N3	2.044(8)	Pd1	N3	2.035(4)
Pd2	N15	2.021(8)	Pd2	N15	2.026(4)
Pd2	N16	2.025(9)	Pd2	N16	2.031(4)
Pd2	N14	2.027(8)	Pd2	N14	2.032(5)
Pd2	N13	2.061(8)	Pd2	N13	2.038(5)

Atom	**Atom**	**Atom**	**Angle/°**	**Atom**	**Atom**	**Atom**	**Angle/°**
N2	Pd1	N1	89.8(3)	N2	Pd1	N1	89.95(16)
N2	Pd1	N4	176.7(3)	N2	Pd1	N4	177.99(16)
N1	Pd1	N4	91.2(3)	N1	Pd1	N4	91.11(16)
N2	Pd1	N3	90.4(3)	N2	Pd1	N3	89.71(15)
N1	Pd1	N3	176.2(3)	N1	Pd1	N3	176.02(16)
N4	Pd1	N3	88.9(3)	N4	Pd1	N3	89.36(15)
N15	Pd2	N16	91.5(3)	N15	Pd2	N16	88.73(18)
N15	Pd2	N14	87.0(3)	N15	Pd2	N14	87.81(17)

N16	Pd2	N14	175.4(4)	N16	Pd2	N14	174.74(17)
N15	Pd2	N13	177.6(4)	N15	Pd2	N13	176.02(17)
N16	Pd2	N13	88.4(3)	N16	Pd2	N13	88.64(18)
N14	Pd2	N13	92.9(3)	N14	Pd2	N13	94.61(18)

4. Void space volume estimation

The size of the central cavity and two outer cavities of the interlocked dimeric cage has been estimated by using the VOIDOO[4] calculations based on the crystal structure of **[3BF_4@MOC-21](BF_4)$_5$**. A virtual probe with a radius of 1.4 Å (default, water sized) was employed. The packing coefficient for BF_4^- and NO_3^- guest anions are estimated with the anion volume referred to the reported values.[5]

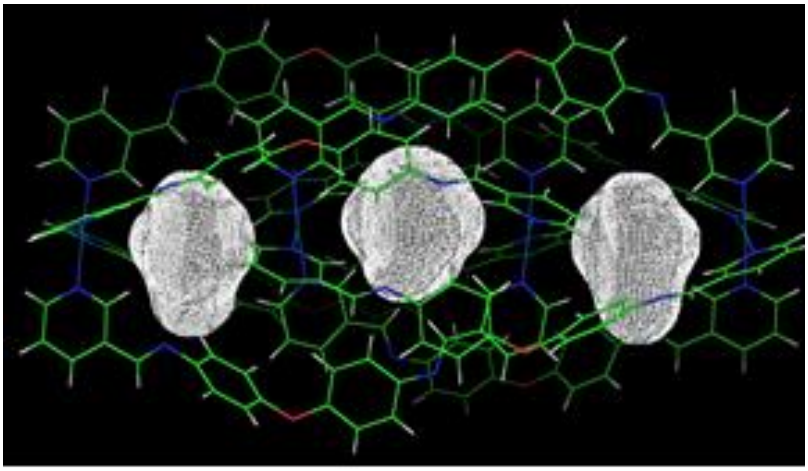

Figure S15. The cavity was visualized as a gray mesh inside the crystal structure of **[3BF_4@MOC-21](BF_4)$_5$**.

Table S6. Volumes of three cavities in **[3BF_4@MOC-21](BF_4)$_5$** and the packing coefficient for tetrafluoroborate and nitrate guests.

	Volume/Å^3	Packing coefficient for BF_4^- (%)	Packing coefficient for NO_3^- (%)*
Outer pocket 1	63	84	65
Central pocket	80	66	51
Outer pocket 2	63	84	65

*Anion volume values are cited from the previous article.[3]

The partially replaced **[2($I_{0.5}$+(BF_4)$_{0.5}$)+BF_4@MOC-21](BF_4)$_5$** cage may reflect the transition state of anion exchange, and reveal comparable packing coefficient (PC) for BF_4^- and I^- guests due to their similar anionic radii (2.16 vs. 2.28 Å). As estimated by using the VOIDOO[4a] calculations based on the crystal structure of **[3BF_4@MOC-21](BF_4)$_5$** (Table S6, Figure S15), the PC of BF_4^- in outer pockets is 84% and that in central pocket is 66%, both significantly beyond the ideal value of 55% proposed by Rebek et al[4b] for the best host-guest binding.

5. Anion exchange study

5.1 Cl^- exchange with the cage $[3BF_4@MOC\text{-}21](BF_4)_5$

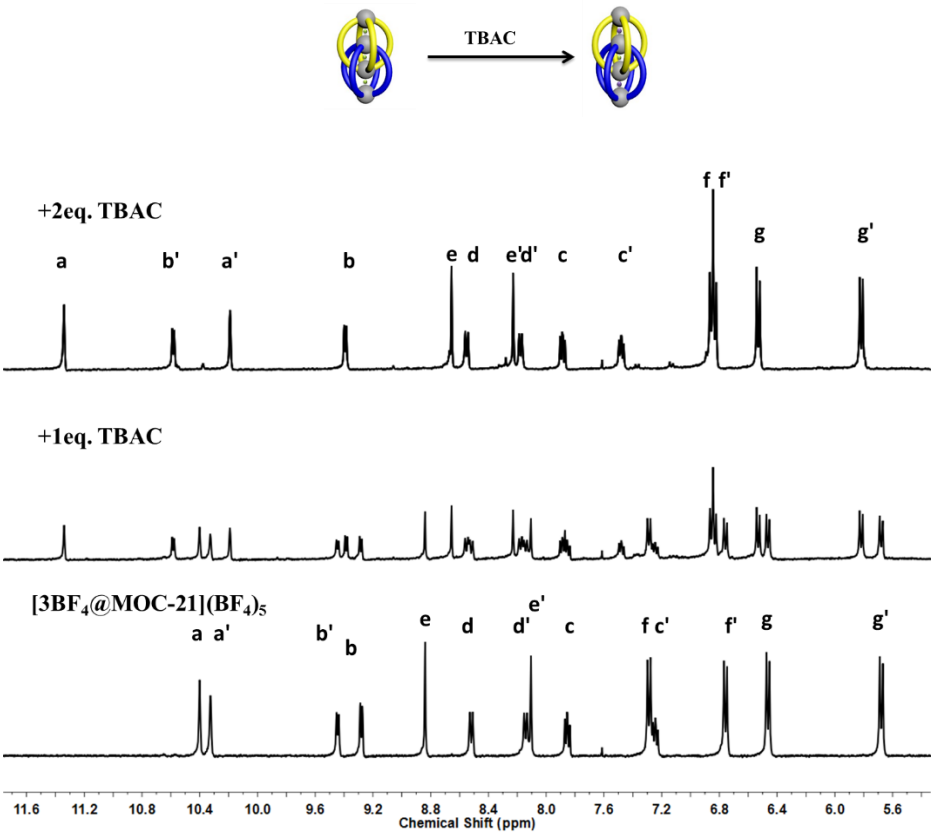

Figure S16. ^1H NMR stack plot for the titration of tetrabutylammonium chloride (Cl^- source) into a solution of cage **$[3BF_4@MOC\text{-}21](BF_4)_5$** (400 MHz, CD_3CN, 298 K).

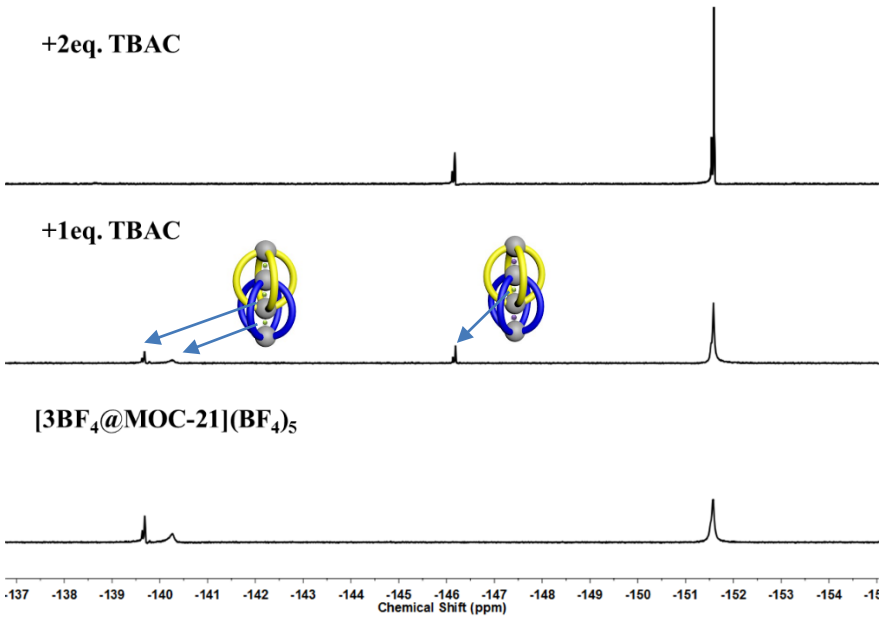

Figure S17. ^{19}F NMR stack plot for the titration of tetrabutylammonium chloride (Cl^- source) into a solution of cage **$[3BF_4@MOC\text{-}21](BF_4)_5$** (376 MHz, CD_3CN, 298 K).

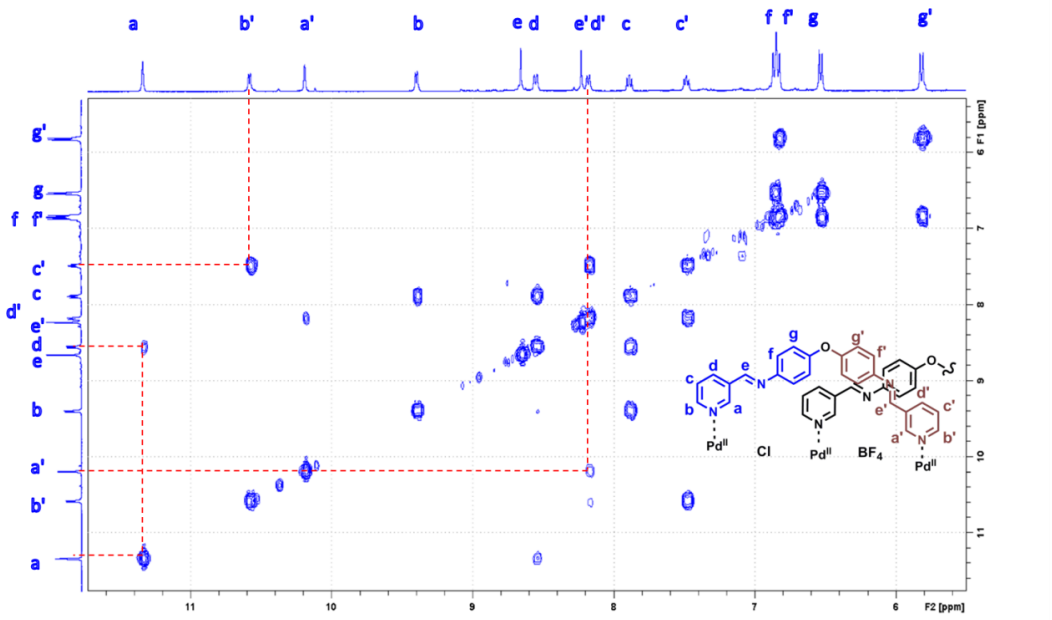

Figure S18. $^{1}H–^{1}H$ COSY spectrum of **[2Cl+BF_4@MOC-21]$^{5+}$** (400 MHz, CD_3CN, 298 K).

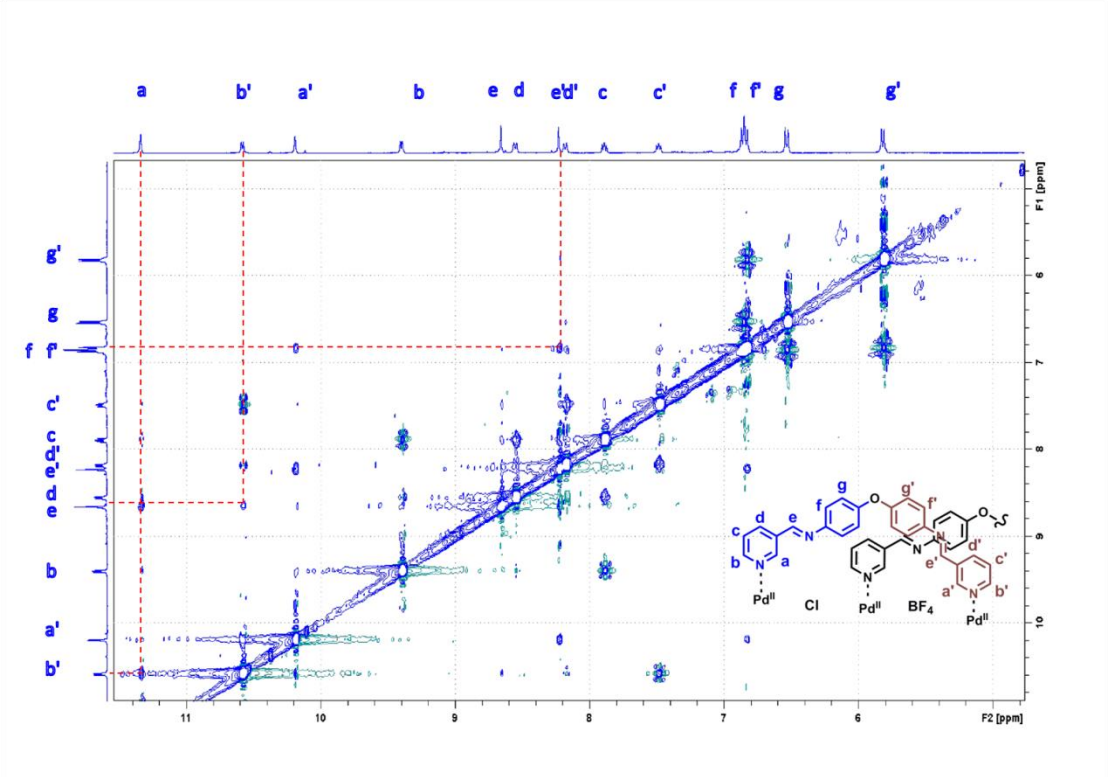

Figure S19. $^{1}H–^{1}H$ NOESY spectrum of **[2Cl+BF_4@MOC-21]$^{5+}$** (400 MHz, CD_3CN, 298 K). The proton which have cross peaks with both H_b and $H_{b'}$ is H_a, therefore we can attribute other peaks.

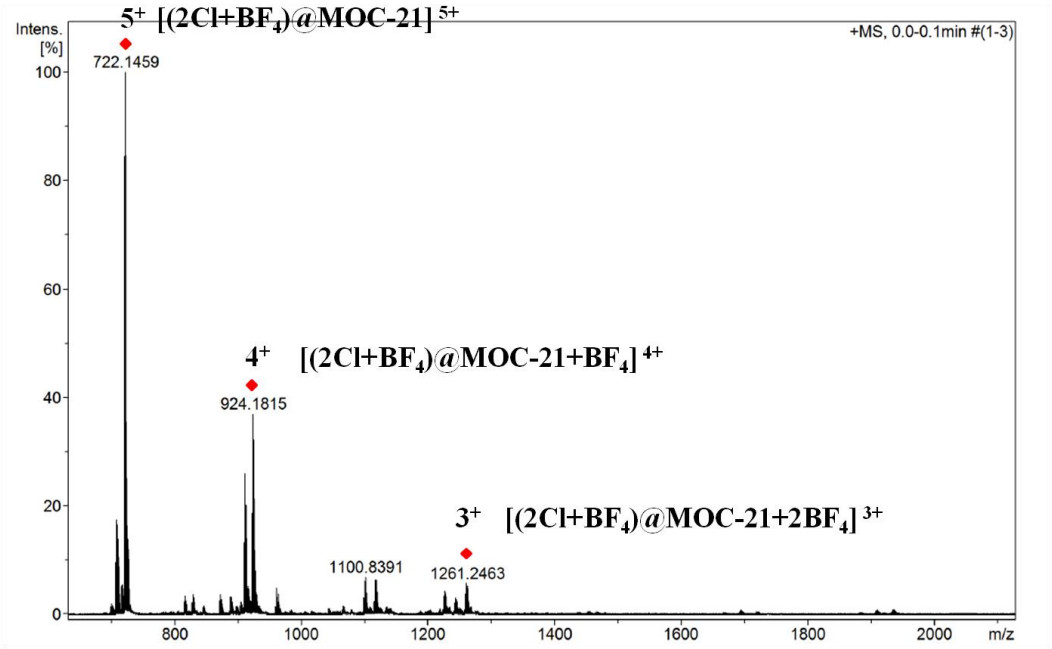

Figure S20. High resolution ESI-mass spectrum for **[2Cl+BF$_4$@MOC-21]$^{5+}$**.

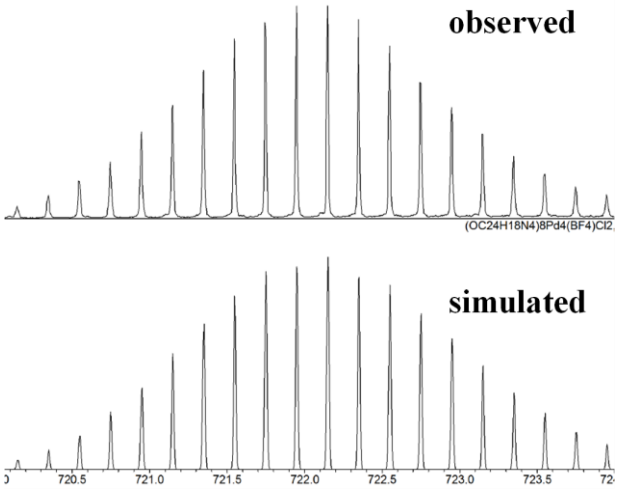

Figure S21. Observed and simulated isotope patterns of 5$^+$ peak of **[2Cl+BF$_4$@MOC-21]$^{5+}$**.

Table S5. Selected mass information in 5$^+$ peaks of **[2Cl+BF$_4$@MOC-21]$^{5+}$**.

Selected mass information in the 5$^+$ peak						
Observed ion (m/z)	**Intensity**	**Resolution**	**FWHM**	**Theoretical mass**	**Difference (obs.–theo.)**	**Error (ppm)**
720.1399	32122	35475	0.0203	720.1488	-0.0089	-12.4
720.3458	58995	37954	0.0190	720.3488	-0.0030	-4.2
720.5472	92617	39965	0.0180	720.5488	-0.0016	-2.2
720.7461	141481	42056	0.0171	720.7488	-0.0027	-3.7
720.9461	213775	46705	0.0154	720.9488	-0.0027	-3.7
721.1457	278617	48319	0.0149	721.1489	-0.0032	-4.4
721.3461	365455	51524	0.0140	721.3489	-0.0028	-3.9

721.5465	442207	54559	0.0132	721.5489	-0.0024	-3.3
721.7463	482428	55484	0.0130	721.7489	-0.0026	-3.6
721.9463	522714	55393	0.0130	721.9490	-0.0027	-3.7
722.1459	523592	59950	0.0120	722.1490	-0.0031	-4.3
722.3462	489203	55969	0.0129	722.3490	-0.0028	-3.9
722.5466	424760	55123	0.0131	722.5491	-0.0025	-3.5
722.7464	336003	50163	0.0144	722.7491	-0.0027	-3.7
722.9464	274545	48767	0.0148	722.9492	-0.0028	-3.9
723.1459	209552	46092	0.0157	723.1493	-0.0034	-4.7
723.3466	155317	44853	0.0161	723.3493	-0.0027	-3.7
723.5469	111103	41060	0.0176	723.5494	-0.0025	-3.5
723.7466	80236	39235	0.0184	723.7495	-0.0029	-4.0
723.9463	59671	38351	0.0189	723.9496	-0.0033	-4.6

5.2 F^- exchange with the cage $[3BF_4@MOC\text{-}21](BF_4)_5$

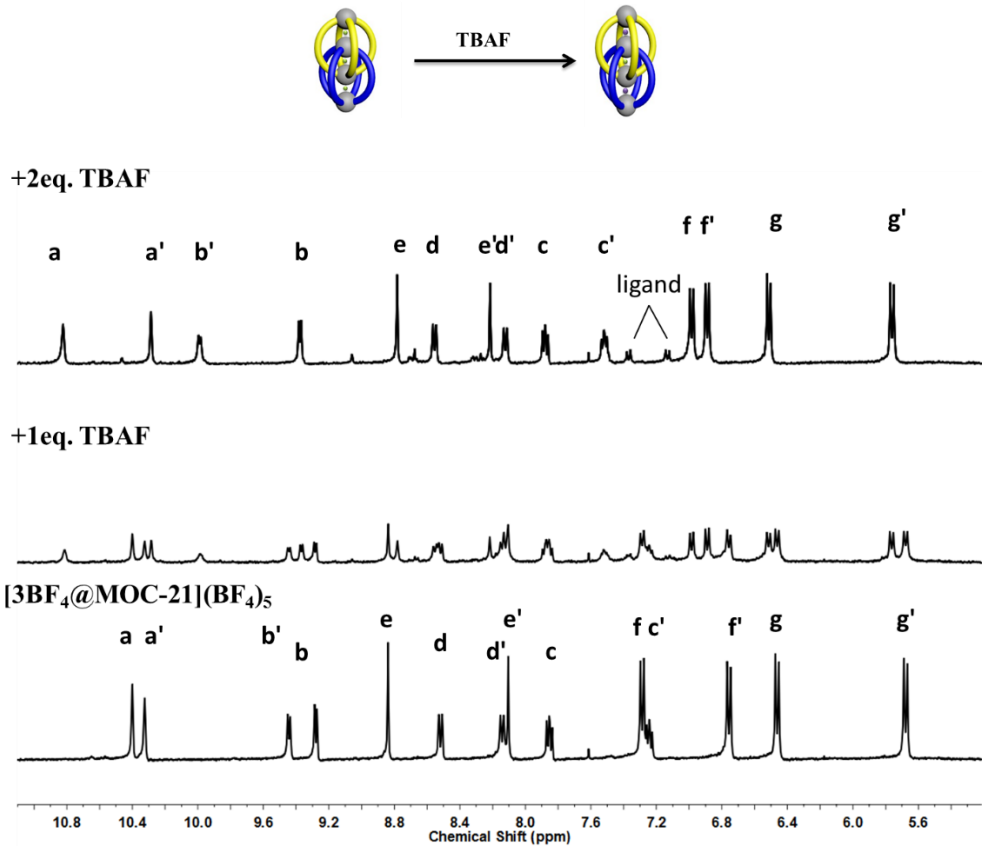

Figure S22. ^1H NMR stack plot for the titration of tetrabutylammonium fluoride (F^- source) into a solution of cage **$[3BF_4@MOC\text{-}21](BF_4)_5$** (400 MHz, CD_3CN, 298 K). Slight decomposition could be observed upon adding the fluoride from NMR.

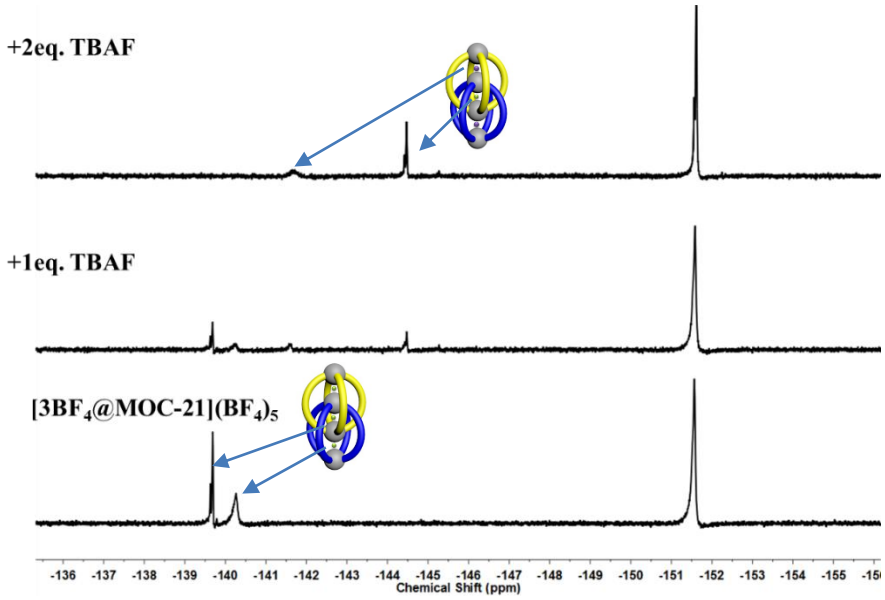

Figure S23. ^{19}F NMR stack plot for the titration of tetrabutylammonium fluoride (F^- source) into a solution of cage **[3BF$_4$@MOC-21](BF$_4$)$_5$** (376 MHz, CD_3CN, 298 K).

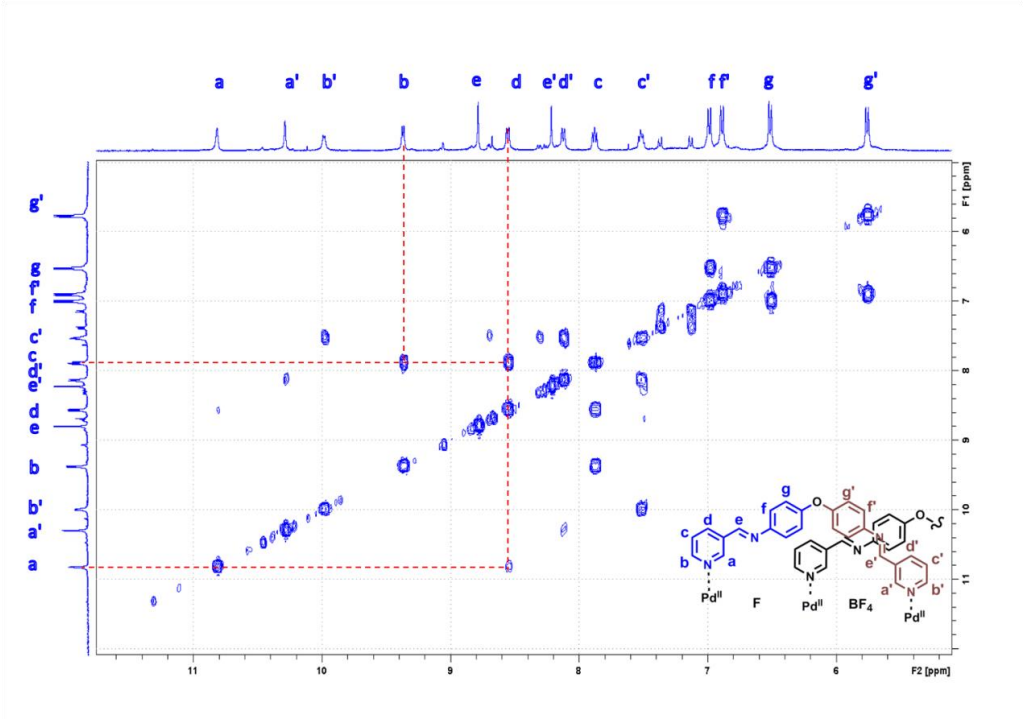

Figure S24. ^{1}H–^{1}H COSY spectrum of **[2F+BF$_4$@MOC-21]$^{5+}$** (400 MHz, CD_3CN, 298 K) , peaks linked by red lines are from the same ligand.

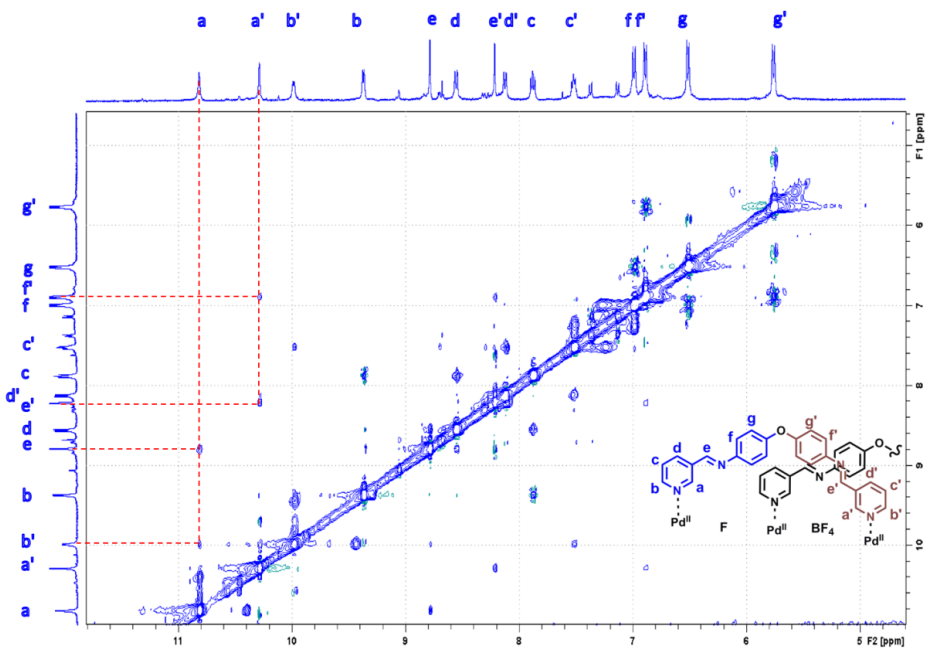

Figure S25. ^{1}H–^{1}H NOESY spectrum of **[2F+BF$_4$@MOC-21]$^{5+}$** (400 MHz, CD_3CN, 298 K), cross peaks could be observed despite some noise signals.

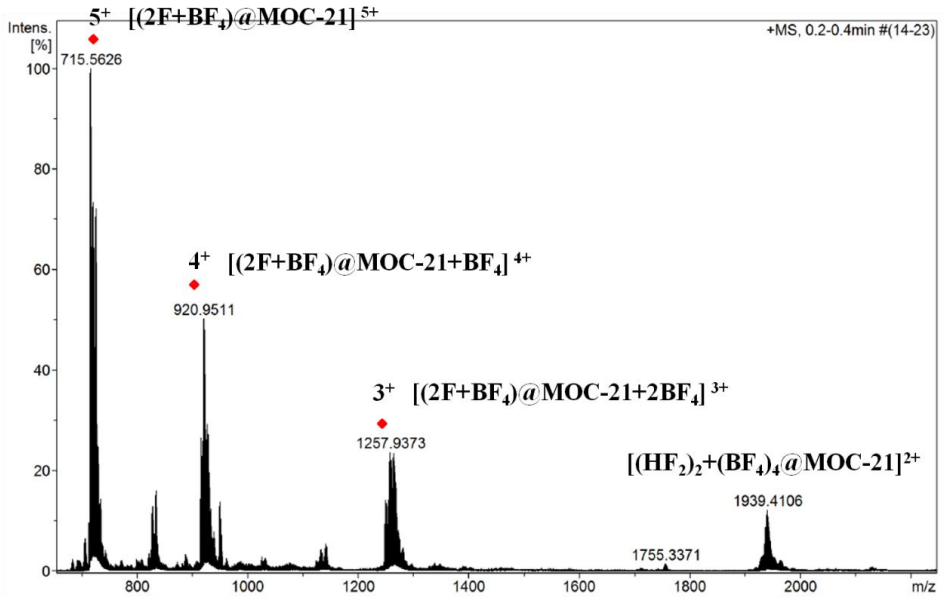

Figure S26. High resolution ESI-mass spectrum for **[2F+BF$_4$@MOC-21]$^{5+}$**.

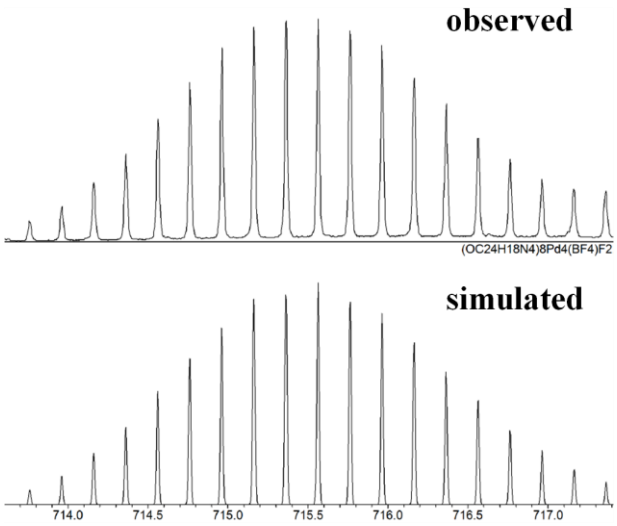

Figure S27. Observed and simulated isotope patterns of 5^+ peak of **[2F+BF$_4$@MOC-21]$^{5+}$**.

Table S6. Selected mass information in 5^+ peaks of **[2F+BF$_4$@MOC-21]$^{5+}$**.

Selected mass information in the 5^+ peak						
Observed ion (m/z)	**Intensity**	**Resolution**	**FWHM**	**Theoretical mass**	**Difference (obs.–theo.)**	**Error (ppm)**
713.9618	16832	31783	0.0225	713.9606	0.0012	1.7
714.1607	28087	32839	0.0217	714.1607	0.0000	0.0
714.3623	42139	33906	0.0211	714.3607	0.0016	2.2
714.5626	58629	35214	0.0203	714.5608	0.0018	2.5
714.7623	75901	36824	0.0194	714.7609	0.0014	2.0
714.9624	92372	37925	0.0189	714.9609	0.0015	2.1
715.1619	102075	37895	0.0189	715.1610	0.0009	1.3
715.3626	105045	37543	0.0191	715.3610	0.0016	2.2
715.5626	106007	37945	0.0189	715.5610	0.0016	2.2
715.7625	100052	37715	0.0190	715.7610	0.0015	2.1
715.9626	93442	37847	0.0189	715.9611	0.0015	2.1
716.1621	77750	36044	0.0199	716.1612	0.0009	1.3
716.3624	65529	35983	0.0199	716.3613	0.0011	1.5
716.5627	49640	33793	0.0212	716.5615	0.0012	1.7
716.7622	39590	33668	0.0213	716.7616	0.0006	0.8
716.9615	29994	31964	0.0224	716.9617	-0.0002	-0.3
717.1576	25419	31235	0.0230	717.1619	-0.0043	-6.0
717.3594	24364	30225	0.0237	717.3620	-0.0026	-3.6

5.3 Br^- exchange with the cage $[3BF_4@MOC\text{-}21](BF_4)_5$

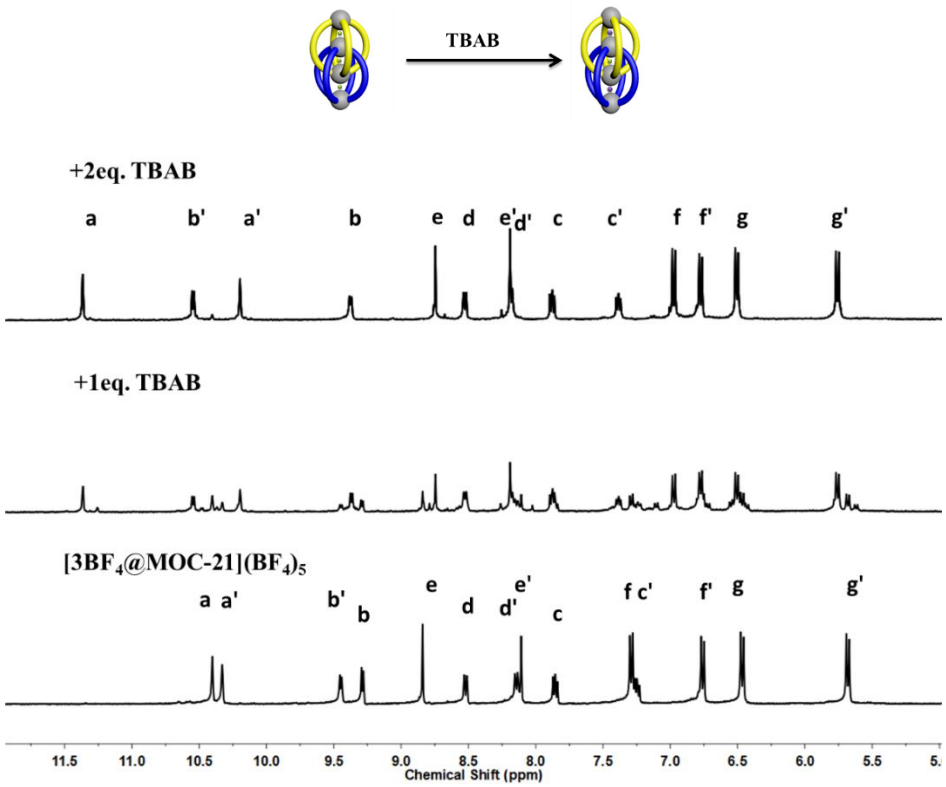

Figure S28. ^1H NMR stack plot for the titration of tetrabutylammonium bromide (Br^- source) into a solution of cage **$[2Br+BF_4@MOC\text{-}21](BF_4)_5$** (400 MHz, CD_3CN, 298 K). Appearance of intermediate **$[Br+2BF_4@MOC\text{-}21](BF_4)_5$** and free **L** is observed when adding 1 equiv. of Br^-.

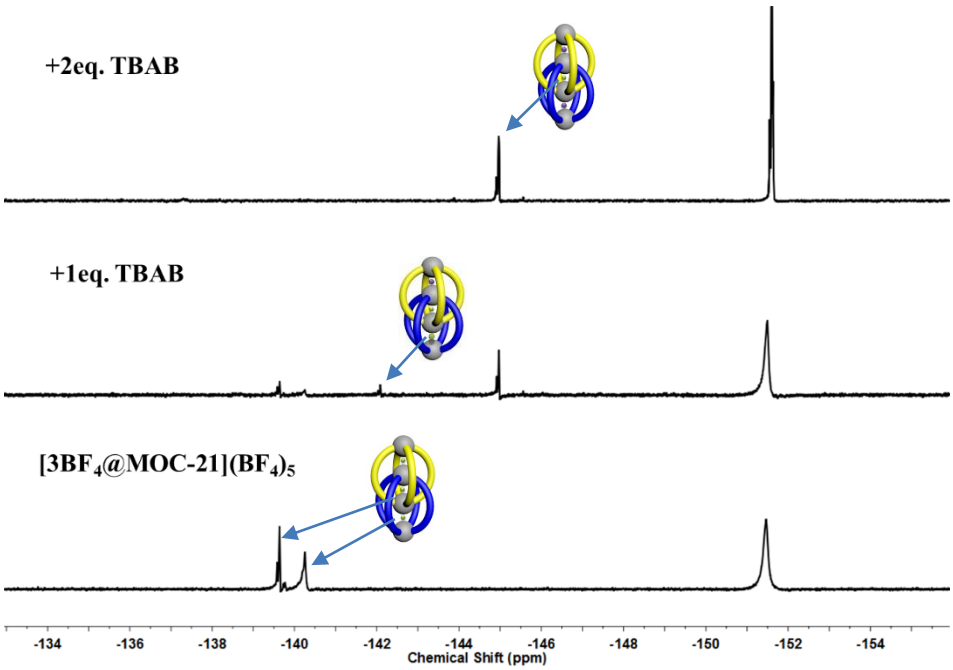

Figure S29. ^{19}F NMR stack plot for the titration of tetrabutylammonium bromide (Br^- source) into a solution of cage **$[2Br+BF_4@MOC\text{-}21](BF_4)_5$** (376 MHz, CD_3CN, 298 K).

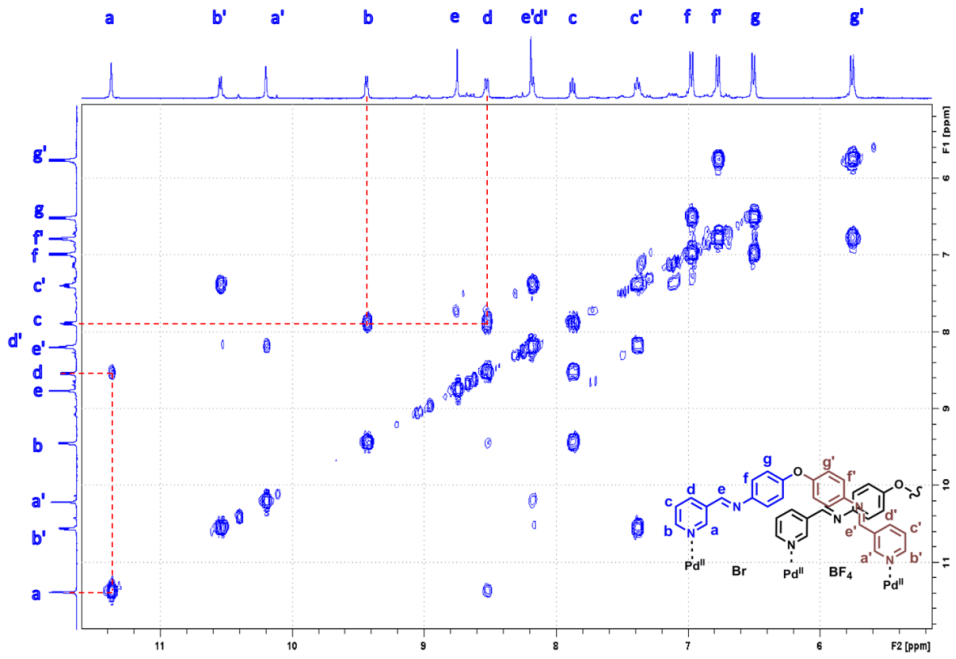

Figure S30. ^{1}H–^{1}H COSY spectrum of **[2Br+BF$_4$@MOC-21]$^{5+}$** (400 MHz, CD_3CN, 298 K), peaks linked by red lines are from the same ligand.

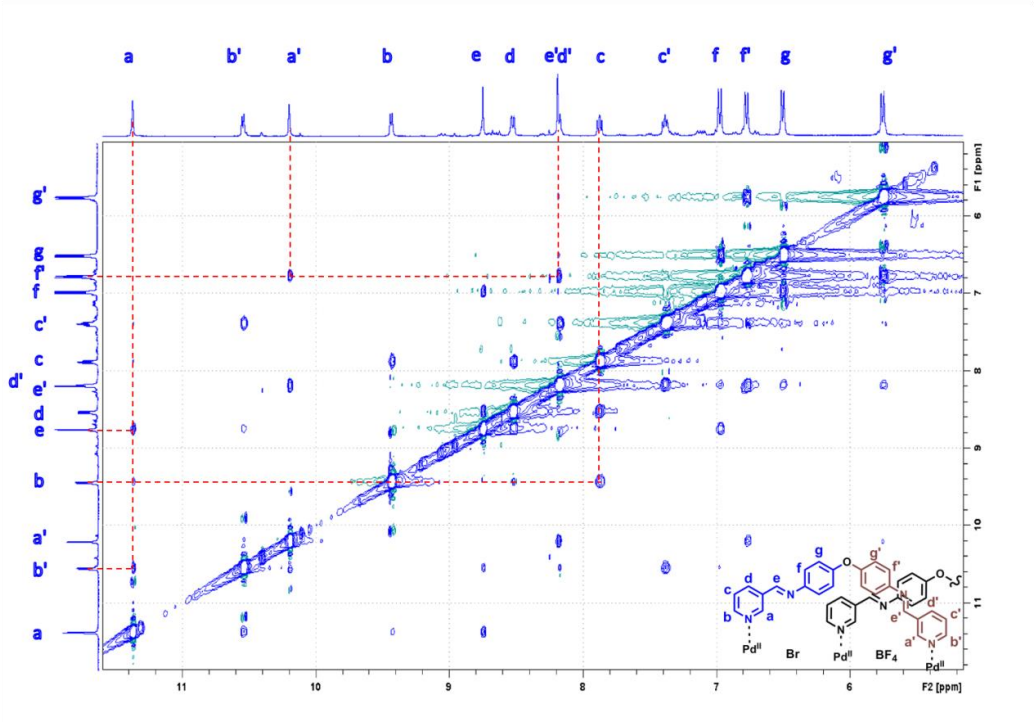

Figure S31. ^{1}H–^{1}H NOESY spectrum of **[2Br+BF$_4$@MOC-21]$^{5+}$** (400 MHz, CD_3CN, 298 K). The proton which have cross peaks with both H_b and $H_{b'}$ is H_a , therefore we can attribute other peaks..

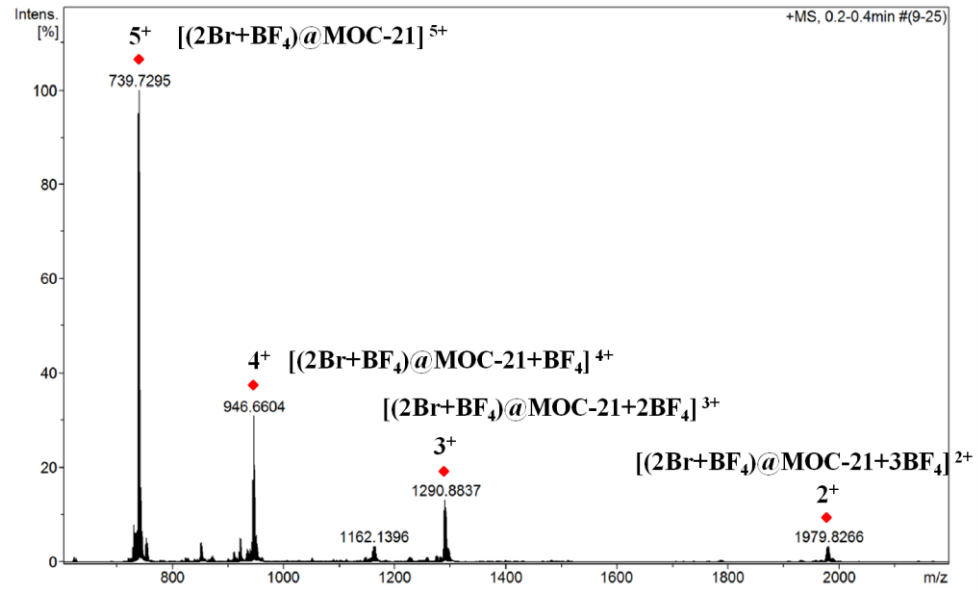

Figure S32. High resolution ESI-mass spectrometry of **[2Br+BF_4@MOC-21](BF_4)$_5$**.

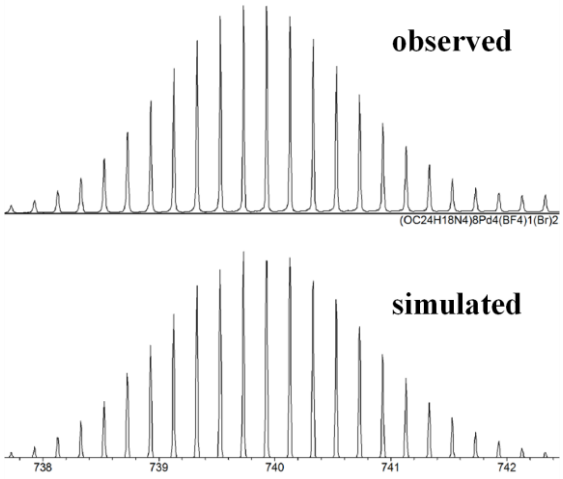

Figure S33. Observed and simulated isotope patterns of 5^+ peak of **[2Br+BF_4@MOC-21]$^{5+}$**.

Table S7. Selected mass information in 5^+ peaks of **[2Br+BF_4@MOC-21]$^{5+}$**.

Selected mass information in the 5^+ peak						
Observed ion (m/z)	**Intensity**	**Resolution**	**FWHM**	**Theoretical mass**	**Difference (obs.–theo.)**	**Error (ppm)**
738.1280	54986	34590	0.0213	738.1285	-0.0005	-0.7
738.3284	86318	36220	0.0204	738.3285	-0.0001	-0.1
738.5289	133213	39861	0.0185	738.5285	0.0004	0.5
738.7289	197053	43296	0.0171	738.7285	0.0004	0.5
738.9291	271447	46794	0.0158	738.9285	0.0006	0.8
739.1292	350582	50559	0.0146	739.1285	0.0007	0.9
739.3293	415179	51590	0.0143	739.3286	0.0007	0.9
739.5295	474792	53771	0.0138	739.5286	0.0009	1.2

739.7295	499300	53969	0.0137	739.7286	0.0009	1.2
739.9296	497694	53803	0.0138	739.9287	0.0009	1.2
740.1296	472462	53790	0.0138	740.1287	0.0009	1.2
740.3296	419264	51982	0.0142	740.3287	0.0009	1.2
740.5296	356297	50849	0.0146	740.5288	0.0008	1.1
740.7296	286632	48426	0.0153	740.7289	0.0007	0.9
740.9295	218768	45704	0.0162	740.9289	0.0006	0.8
741.1295	162949	43092	0.0172	741.1290	0.0005	0.7
741.3295	117989	40434	0.0183	741.3291	0.0004	0.5
741.5297	83806	37697	0.0197	741.5292	0.0005	0.7

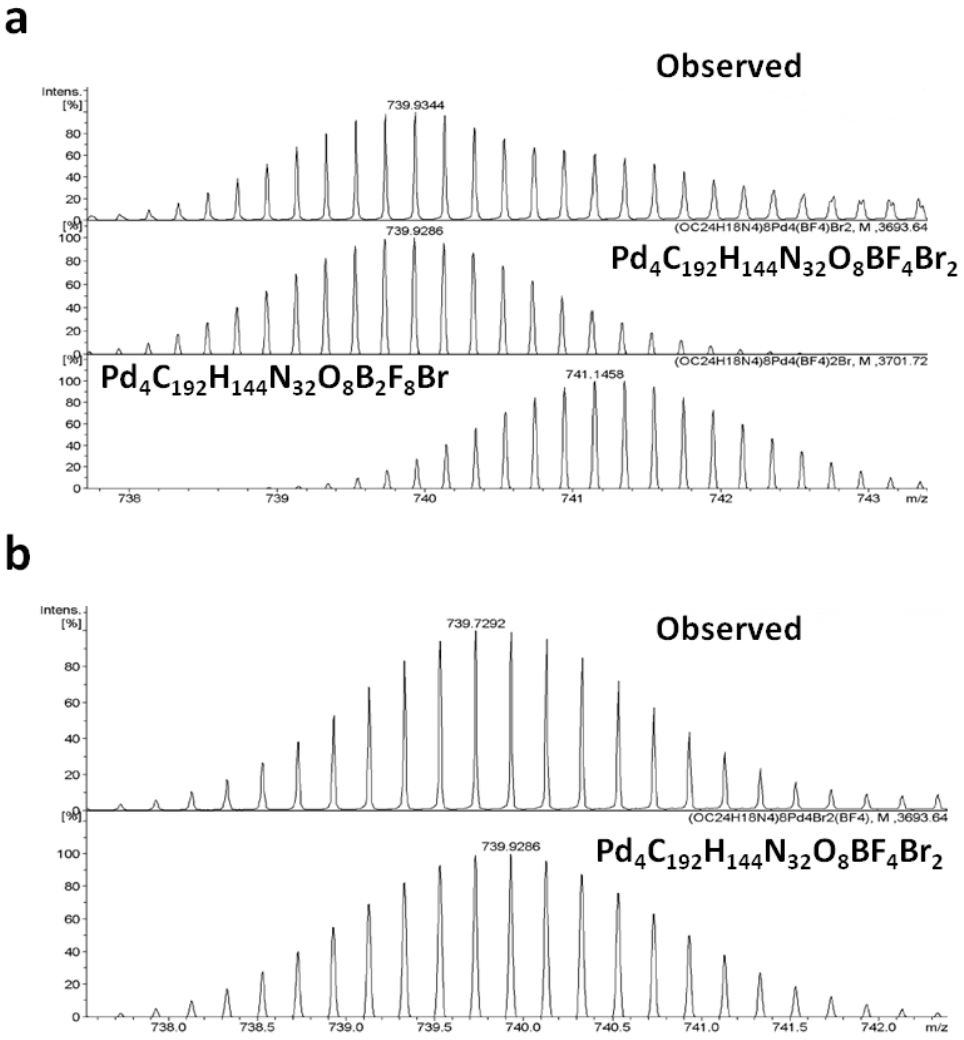

Figure S34. High resolution ESI-mass spectrometry of a) **[3BF$_4$@MOC-21](BF$_4$)$_5$** + 1equiv.TBAB showing the +5 peaks which match the theoretical isotope patterns of **[Br+2BF$_4$@MOC-21]$^{5+}$** and **[2Br+BF$_4$@MOC-21]$^{5+}$**; b) **[3BF$_4$@MOC-21](BF$_4$)$_5$** + 2equiv.TBAB showing +5 peak which matches only the theoretical isotope pattern of **[2Br+BF$_4$@MOC-21]$^{5+}$**.

5.4 I^- exchange with the cage $[3BF_4@MOC\text{-}21](BF_4)_5$ using *n*-Bu_4NI as I^- source

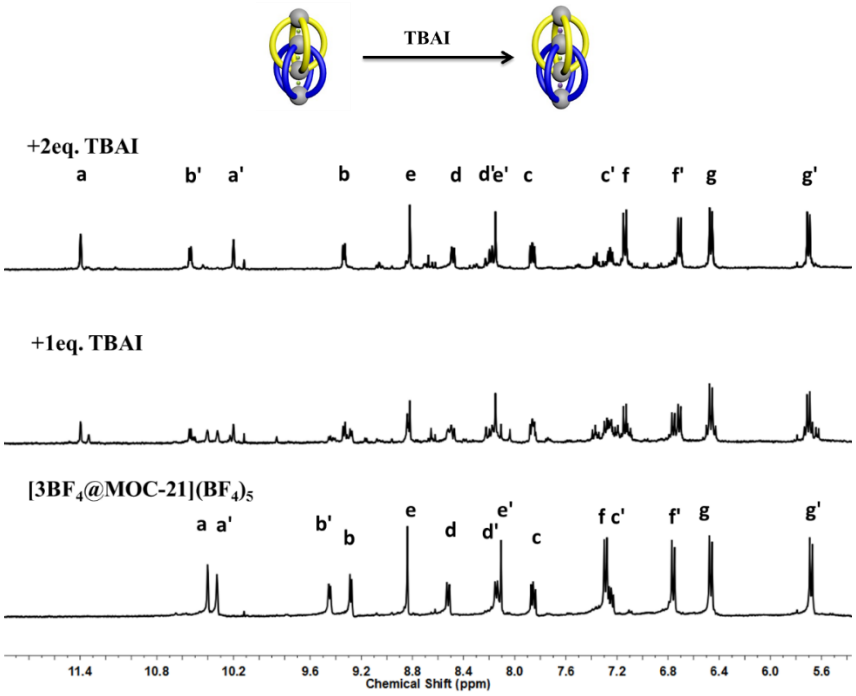

Figure S35. ^1H NMR stack plot for the titration of tetrabutylammonium iodide (I^- source) into a solution of cage **$[3BF_4@MOC\text{-}21](BF_4)_5$** (400 MHz, CD_3CN, 298 K). Appearance of intermediate **$[I+2BF_4@MOC\text{-}21](BF_4)_5$** and free **L** is observed during titration.

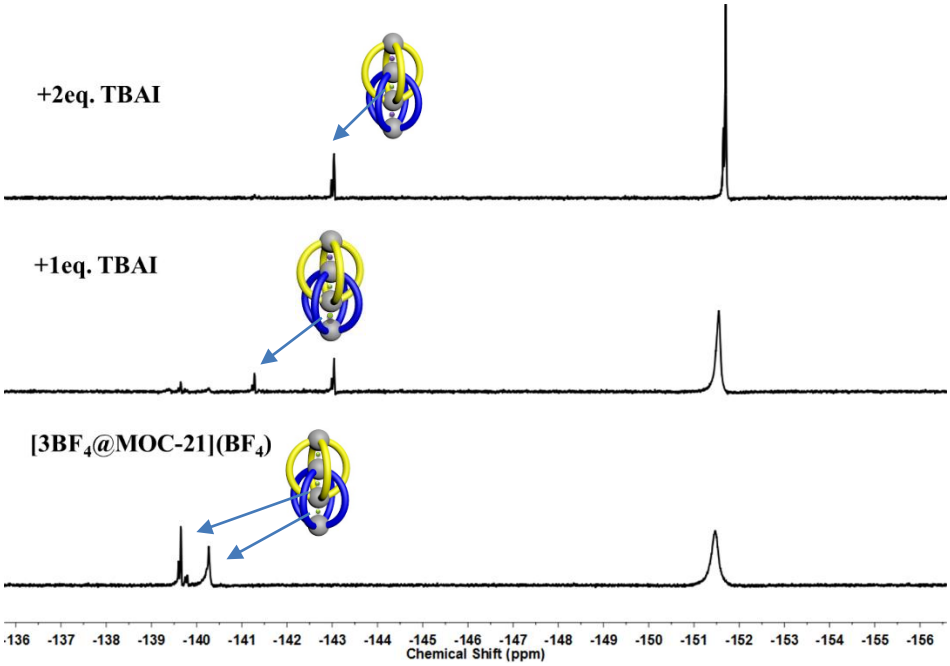

Figure S36. ^{19}F NMR stack plot for the titration of tetrabutylammonium iodide (I^- source) into a solution of cage **$[3BF_4@MOC\text{-}21](BF_4)_5$** (376 MHz, CD_3CN, 298 K).

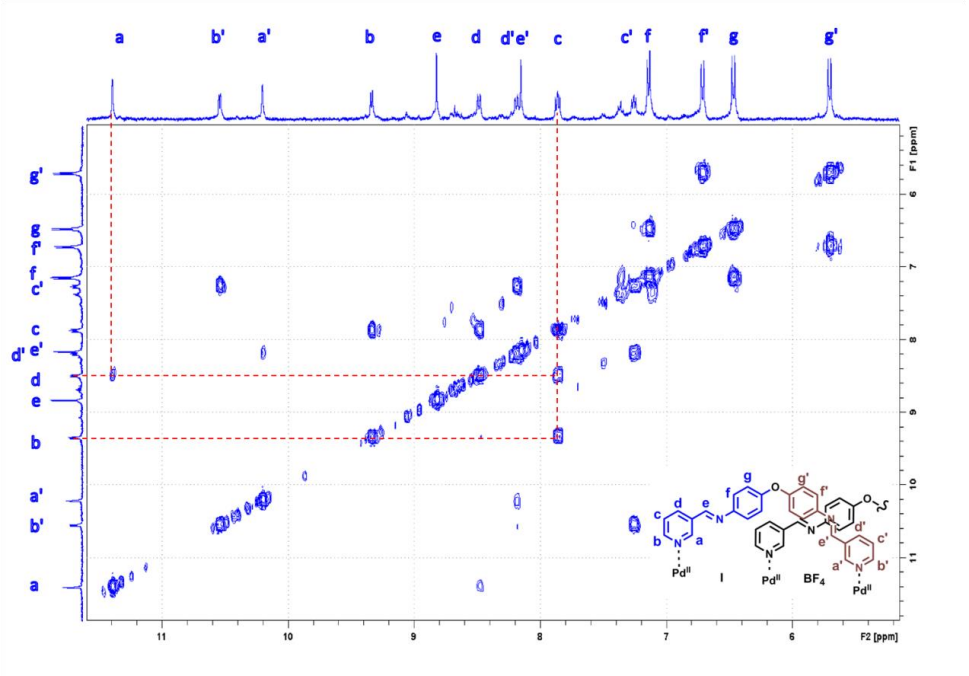

Figure S37. ^{1}H–^{1}H COSY spectrum of **[2I+BF_4@MOC-21]$^{5+}$** (400 MHz, CD_3CN, 298 K), peaks linked by red lines are from the same ligand.

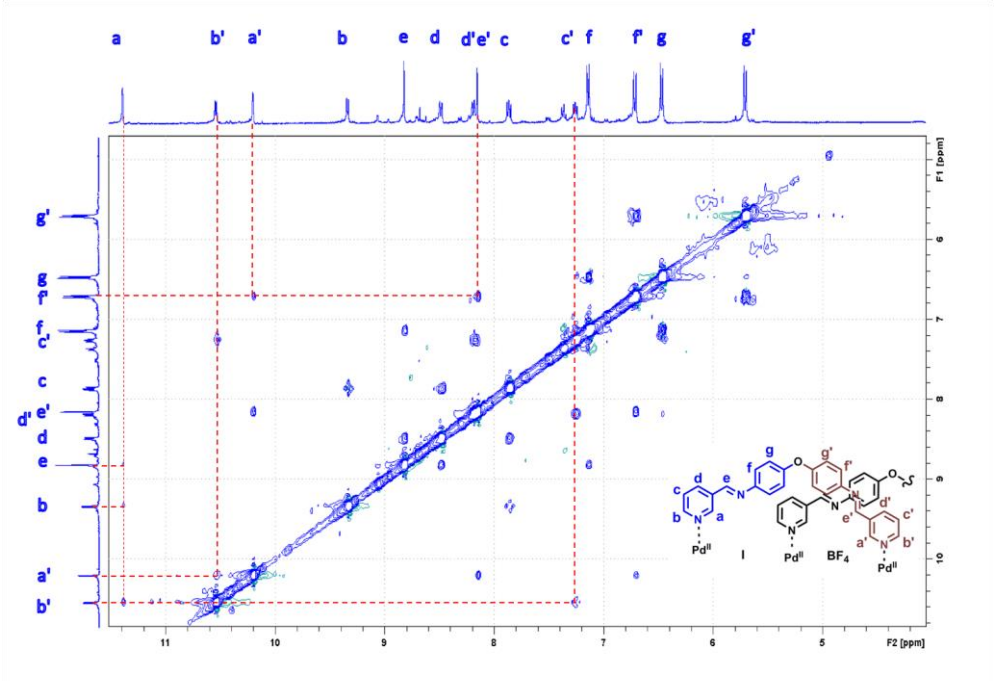

Figure S38. ^{1}H–^{1}H NOESY specturm of **[2I+BF_4@MOC-21]$^{5+}$** (400 MHz, CD_3CN, 298 K). The proton which have cross peaks with both H_b and $H_{b'}$ is H_a , therefore we can attribute other peaks.

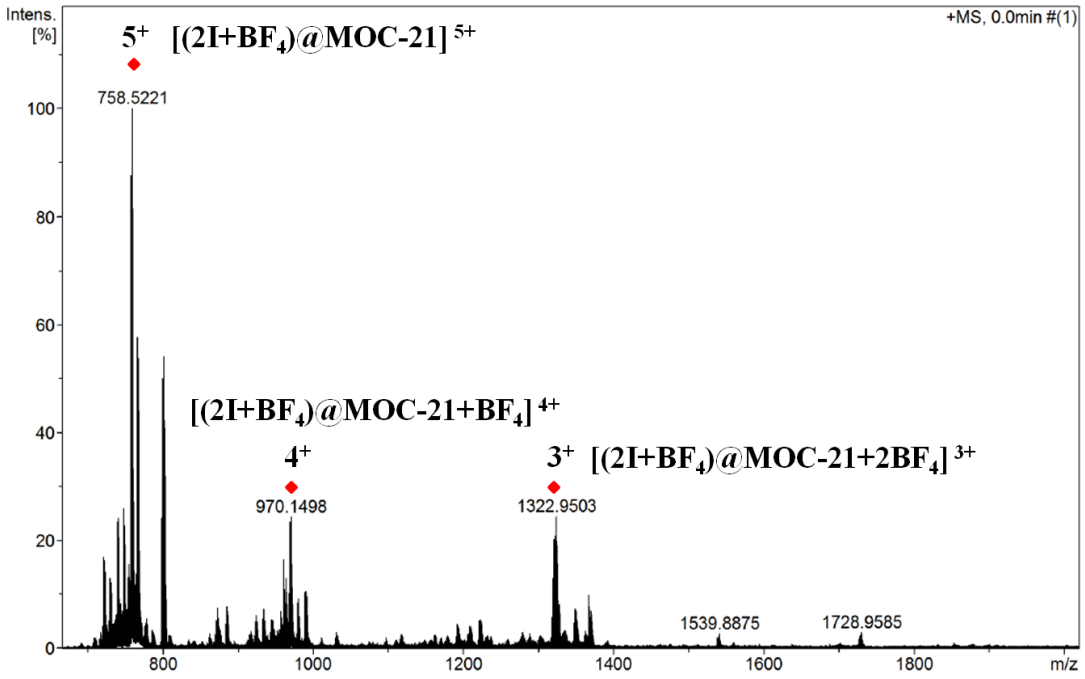

Figure S39. High resolution ESI-mass spectrometry of **[3BF$_4$@MOC-21](BF$_4$)$_5$** + 2equiv.TBAI

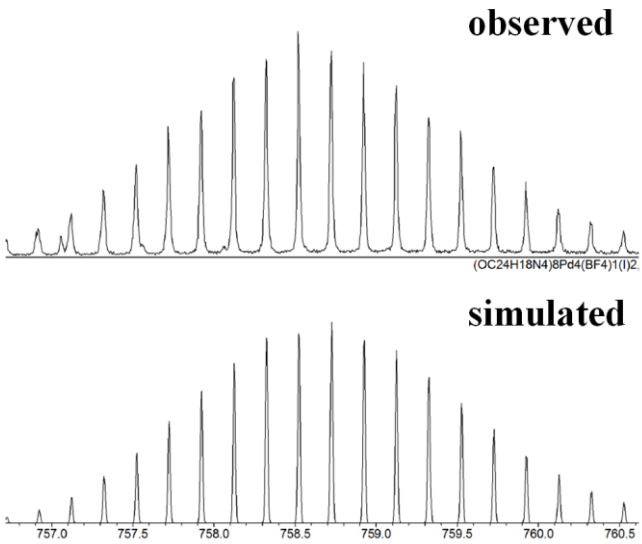

Figure S40. Observed and simulated isotope patterns of 5$^+$ peak of **[2I+BF$_4$@MOC-21]$^{5+}$**.

Table S8. Selected mass information for 5$^+$ peaks of **[2I+BF$_4$@MOC-21]$^{5+}$**.

Selected mass information in the 5$^+$ peak						
Observed ion (m/z)	**Intensity**	**Resolution**	**FWHM**	**Theoretical mass**	**Difference (obs.–theo.)**	**Error (ppm)**
756.9141	16484	22753	0.0333	756.9231	-0.0090	-11.9
757.1063	25440	27724	0.0273	757.1231	-0.0168	-22.2
757.3182	38768	31803	0.0238	757.3232	-0.0050	-6.6

757.5219	53392	34538	0.0219	757.5232	-0.0013	-1.7
757.7199	75200	42040	0.0180	757.7232	-0.0033	-4.4
757.9200	84008	36340	0.0209	757.9233	-0.0033	-4.4
758.1206	103188	39601	0.0191	758.1233	-0.0027	-3.6
758.3212	113616	39462	0.0192	758.3234	-0.0022	-2.9
758.5221	129592	46881	0.0162	758.5235	-0.0014	-1.8
758.7215	118540	43014	0.0176	758.7235	-0.0020	-2.6
758.9218	111728	40729	0.0186	758.9236	-0.0018	-2.4
759.1217	98312	39596	0.0192	759.1237	-0.0020	-2.6
759.3218	80244	39240	0.0194	759.3238	-0.0020	-2.6
759.5221	72544	42399	0.0179	759.5238	-0.0017	-2.2
759.7215	52032	37662	0.0202	759.7239	-0.0024	-3.2
759.9220	43280	42524	0.0179	759.9240	-0.0020	-2.6
760.1211	27656	33729	0.0225	760.1242	-0.0031	-4.1
760.3218	20572	34120	0.0223	760.3243	-0.0025	-3.3

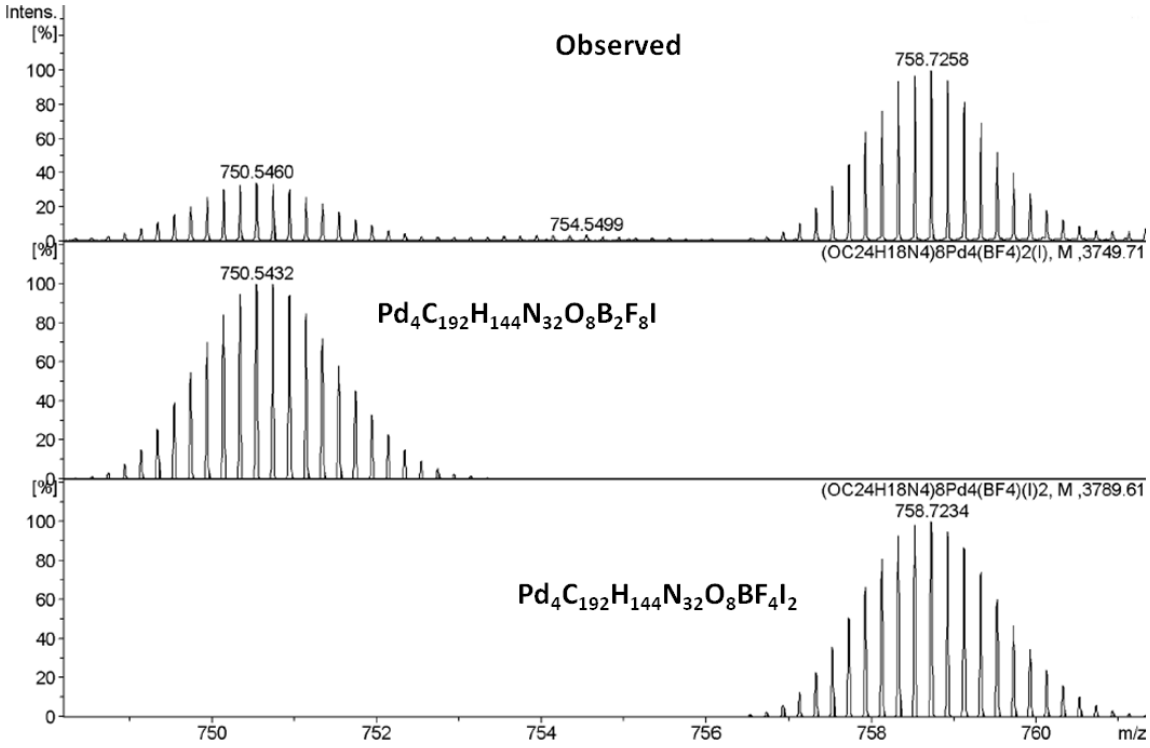

Figure S41. High resolution ESI-mass spectrometry of **[3BF$_4$@MOC-21](BF$_4$)$_5$** + 1equiv.TBAI showing the +5 peaks which match the theoretical isotope patterns of **[I+2BF$_4$@MOC-21]$^{5+}$** and **[2I+BF$_4$@MOC-21]$^{5+}$**.

5.5 I^- exchange with the cage $[3BF_4@MOC\text{-}21](BF_4)_5$ using *n*-Bu_4NI_3 as I^- source

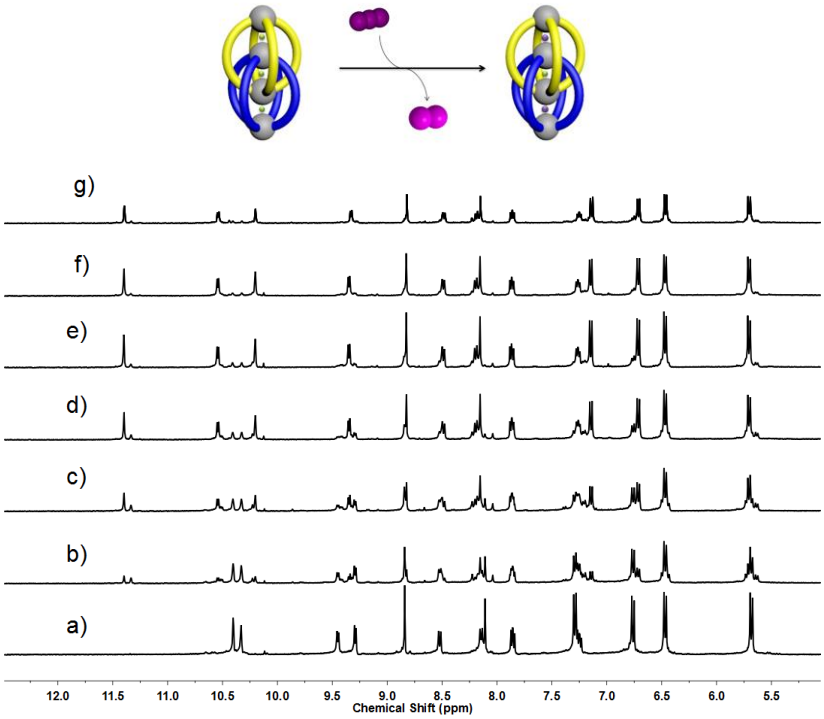

Figure S42. Stoichiometric addition of tetrabutylammonium triiodide (I^- source) to a solution of **$[3BF_4@MOC\text{-}21](BF_4)_5$** (298K, 400MHz, CD_3CN). (a) **$[3BF_4@MOC\text{-}21](BF_4)_5$**, (b) addition of 1 equiv., (c) 2 equiv., (d) 3 equiv., (e) 4 equiv., (f) 5 equiv. of I_3^-, and (g) **$[2I{+}BF_4@MOC\text{-}21]^{5+}$** for comparison.

5.6 NO_3^- exchange with the cage $[3BF_4@MOC\text{-}21](BF_4)_5$ to displace all BF_4^-

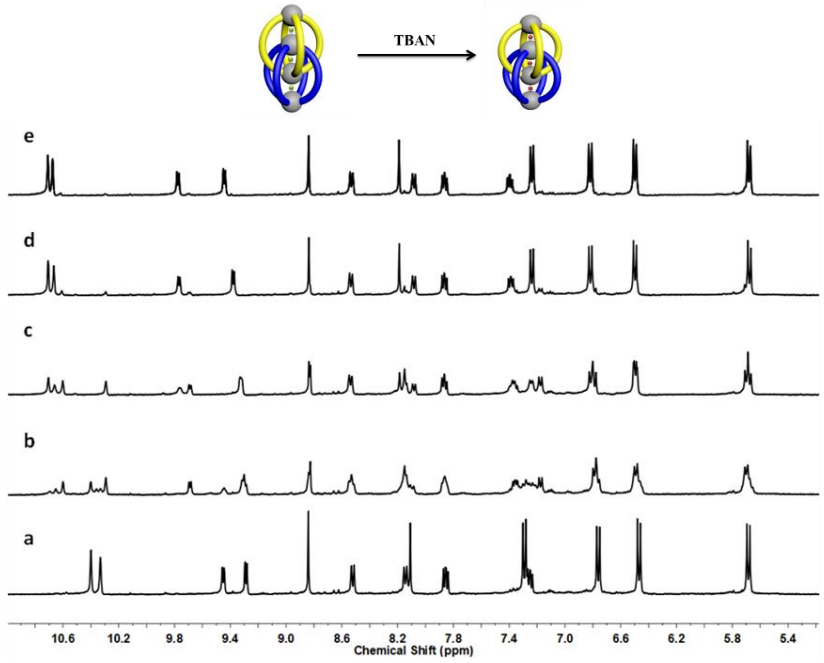

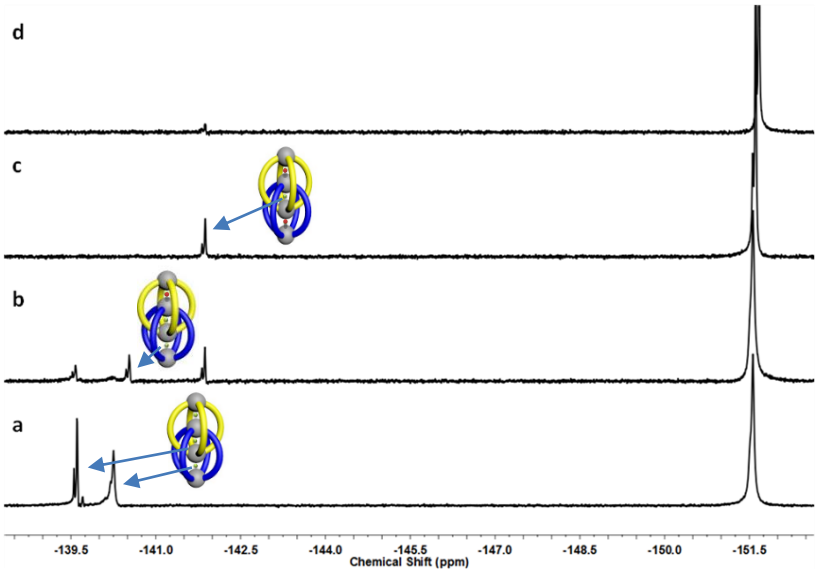

Figure S43. Top: Stoichiometric addition of tetrabutylammonium nitrate to a CD_3CN solution of **[3BF$_4$@MOC-21](BF$_4$)$_5$** (298K, 400MHz, CD_3CN). (a) **[3BF$_4$@MOC-21](BF$_4$)$_5$**, (b) addition of 1.2 equiv., (c) 2.4 equiv., (d) 3.6 equiv. tetrabutylammonium nitrate and (e) spectrum of **[3BF$_4$@MOC-21]**$^{5+}$ for comparison. Bottom: (a) ^{19}F NMR of **[3BF$_4$@MOC-21](BF$_4$)$_5$**, (b) addition of 1.2 equiv., (c) 2.4 equiv., (d) 3.6 equiv. tetrabutylammonium nitrate (376 MHz, CD_3CN, 298 K).

5.7 Cl^- exchange with the cage [3NO$_3$@MOC-21](NO$_3$)$_5$

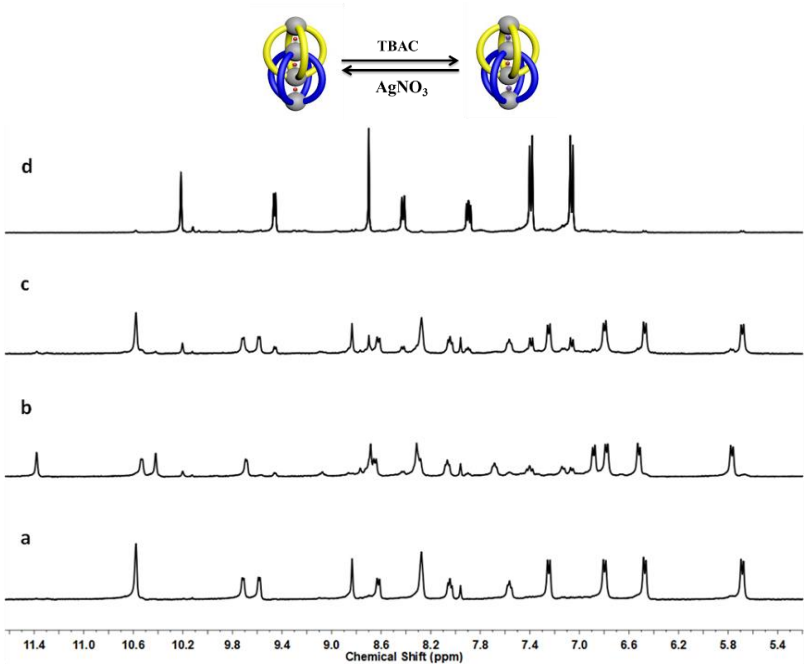

Figure S44. ^{1}H NMR spectrum of (a) **[3NO$_3$@MOC-21](NO$_3$)$_5$**, (b) addition of 2 equiv. tetrabutylammonium chloride (Cl^- source), (c) addition of 2 equiv. $AgNO_3$, and (d) **[MOC-20](NO$_3$)$_4$** for comparison (400 MHz, DMSO-d_6, 298 K), showing appearance of trace **[MOC-20](NO$_3$)$_4$** during the anion exchange.

5.8 Br^- exchange with the cage $[3NO_3@MOC\text{-}21](NO_3)_5$

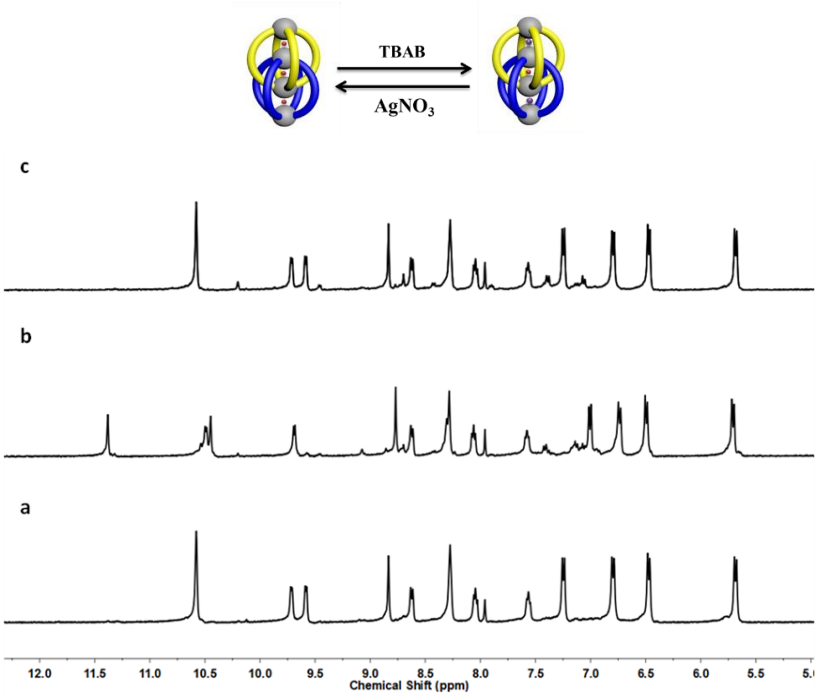

Figure S45. ^{1}H NMR spectrum of (a) **$[3NO_3@MOC\text{-}21](NO_3)_5$**, (b) addition of 2 equiv. tetrabutylammonium bromide (Br^- source), (c) addition of 2 equiv. $AgNO_3$ (400 MHz, DMSO-d_6, 298 K).

5.9 F^- exchange with the cage $[3NO_3@MOC\text{-}21](NO_3)_5$

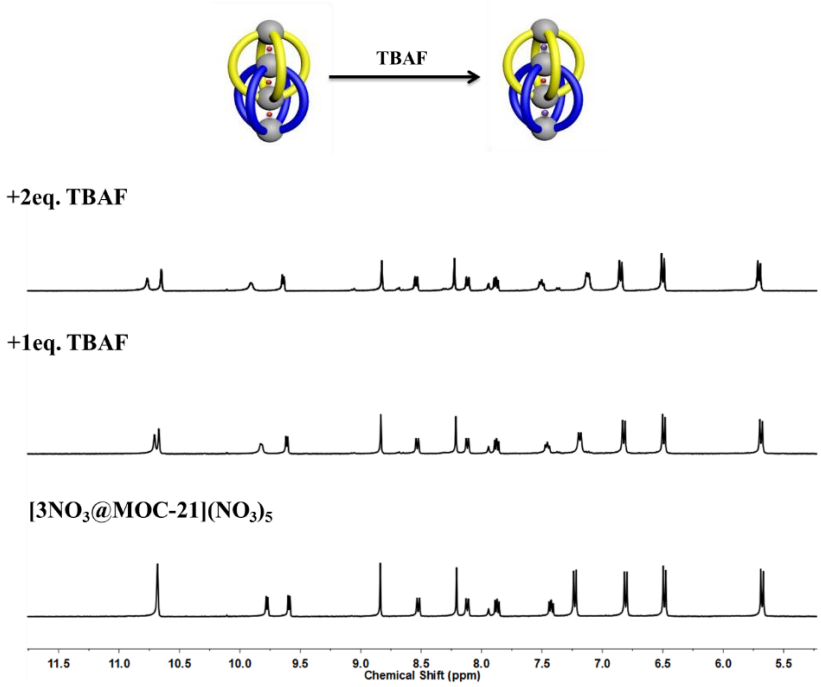

Figure S46. ^{1}H NMR stack plot for the titration of tetrabutylammonium fluoride (F^- source) into a solution of cage **$[3NO_3@MOC\text{-}21](NO_3)_5$** ($CD_3CN$:DMSO-$d_6$ = 7:1, v/v), showing fast anion exchange upon addition of F^- anions (400 MHz, 298 K).

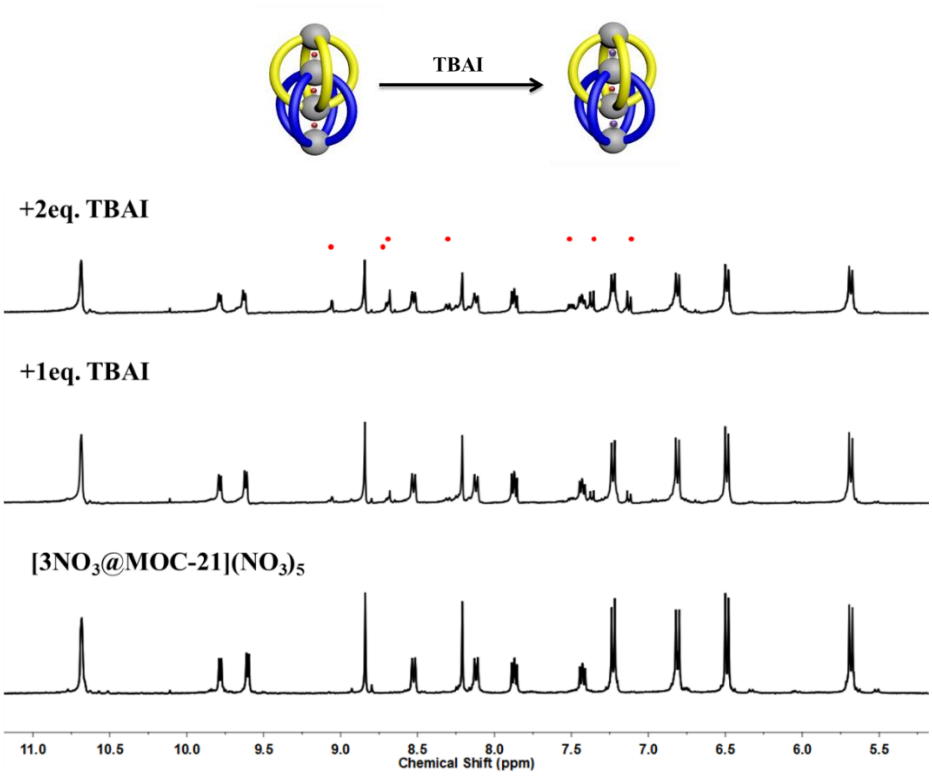

Figure S47. ^{1}H NMR stack plot for the titration of tetrabutylammonium iodide (I^- source) into a solution of cage **[3NO$_3$@MOC-21](NO$_3$)$_5$** (CD_3CN:DMSO-d_6 = 9:1, v/v), showing partial decomposition of the cage denoted by the red circles.

5.10 F^- vs. Br^- competitive binding study

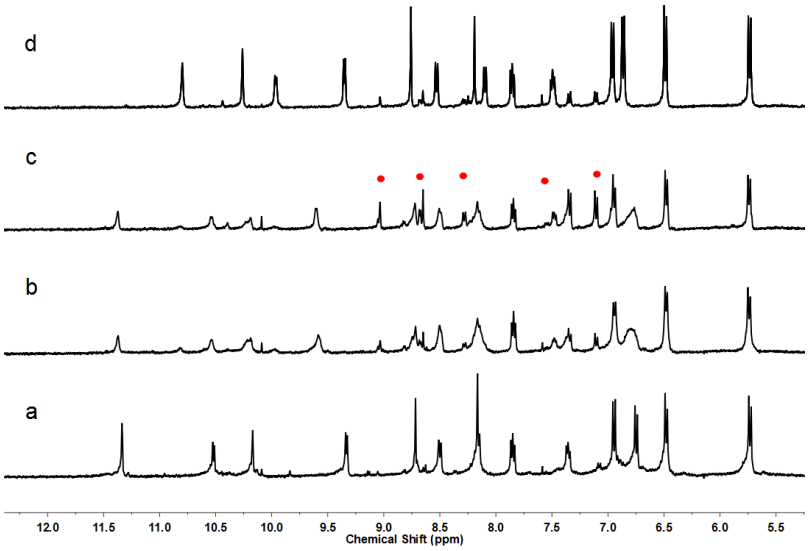

Figure S48. ^{1}H NMR spectra of (a) **[2Br+BF$_4$@MOC-21]$^{5+}$**, (b) addition of 2 equiv. *n*-Bu_4NF to a solution of **[2Br+BF$_4$@MOC-21]$^{5+}$**, (c) addition of 2 equiv. *n*-Bu_4NBr to a solution of **[2F+BF$_4$@MOC-21]$^{5+}$**, and (d) **[2F+BF$_4$@MOC-21]$^{5+}$**. Red circles denote ligand **L** (400 MHz, CD_3CN, 298 K).

5.11 F^- vs. I^- competitive binding study

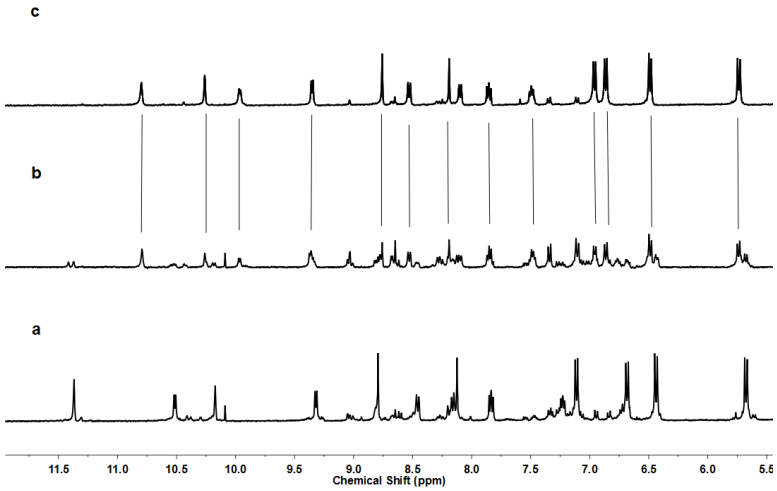

Figure S49. ^{1}H NMR spectra of (a) **[2I+BF$_4$@MOC-21]$^{5+}$**, (b) addition of 2 equiv. *n*-Bu$_4$NF to a solution of **[2I+BF$_4$@MOC-21]$^{5+}$**, (c) **[2F+BF$_4$@MOC-21]$^{5+}$** for comparison (400 MHz, CD_3CN, 298 K).

6. Anion binding constant and Gibbs free energy determination

6.1 Binding affinity for Cl^- over BF_4^- with the interlocked cage

The method to measuring binding constants for chloride over tetrafluoroborate guests by the dimeric interlocked cage is adapted from previous report by others.[6] The only difference is that herein we take into account the tetrafluoroborate anions inside the cavities. **[2Cl+BF$_4$@MOC-21](BF$_4$)$_5$** (0.77 mM) was prepared by addition two equivalent tetrabutylammonia chloride (97.3 mM, CD_3CN) to an acetonitrile-d_3 solution of **[3BF$_4$@MOC-21](BF$_4$)$_5$ (**0.78 mM) in a NMR tube. Small aliquots of the $AgBF_4$ solution were titrated into this NMR tube. ^{1}H NMR spectra were recorded 15 minutes later so that the solution could equilibrate at room temperature.

[3BF$_4$@MOC-21]$^{5+}$ + 2Cl$^-$ → [2Cl+BF$_4$@MOC-21]$^{5+}$ + 2BF$_4^-$

The apparent binding constant K_a for this exchange reaction can be expressed as:

$$K_a^{Cl/BF_4} = \frac{[\mathbf{2Cl+BF_4@MOC-21}]\cdot[BF_4^-]^2}{[\mathbf{3BF_4@MOC-21}]\cdot[Cl^-]^2} \qquad \text{(S1)}$$

The concentration of the free Cl^- was obtained from the solubility[7] K_{sp}^{AgCl} of AgCl. **[2Cl+BF$_4$@MOC-21]$^{5+}$** equals to **[3BF$_4$@MOC-21](BF$_4$)$_5$** at the middle point of the titration, then the equation (S1) can be simplified as:

$$K_a^{Cl/BF_4} = \frac{[Ag^+]^2\cdot[BF_4^-]^2}{K_{sp}^{AgCl\,2}} \qquad \text{(S2)}$$

We derived the middle point of the titration to be 4.9 equiv. (8.06 μL) of $AgBF_4$ *via* interpolation method. At the middle point, the concentration of the host was diluted from 0.90

mM to 0.87 mM.

Based the NMR titration results, $[Ag^+]$ and $[BF_4^-]$ were calculated as:

$$[Ag^+] = (4.9 - 1) \times 0.87\ \text{mM} = 3.39\ \text{mM} \quad \text{(S3)}$$

$$[BF_4^-] = (4.9 + 7 - 2 \cdot 0.5) \cdot 0.87\ \text{mM} = 9.48\ \text{mM} \quad \text{(S4)}$$

Inserting equation S3 and S4 in S2 yields:

$$K_a^{Cl/BF_4} = 6.5\times10^{15}$$

It is worth noting that we only obtained an apparent binding constant for $[HG_2]$ complex (**[2Cl+BF$_4$@MOC-21]$^{5+}$**) under the circumstances that [HG] complex (**[Cl+2BF$_4$@MOC-21]$^{5+}$**) cannot be detected on ^{1}H NMR, which is true in the present case according to the NMR titration result. This binding behavior clearly indicates strong positive cooperative. The Gibbs free energy for this anion exchange reaction could be estimated as:

$$\Delta G_{ex}^{Cl/BF_4} = -\mathrm{RT}\ln K_a^{Cl/BF_4} = -8.314\times298\times\ln K_a^{Cl/BF_4} = -90.2\ \ \text{kJ mol}^{-1}$$

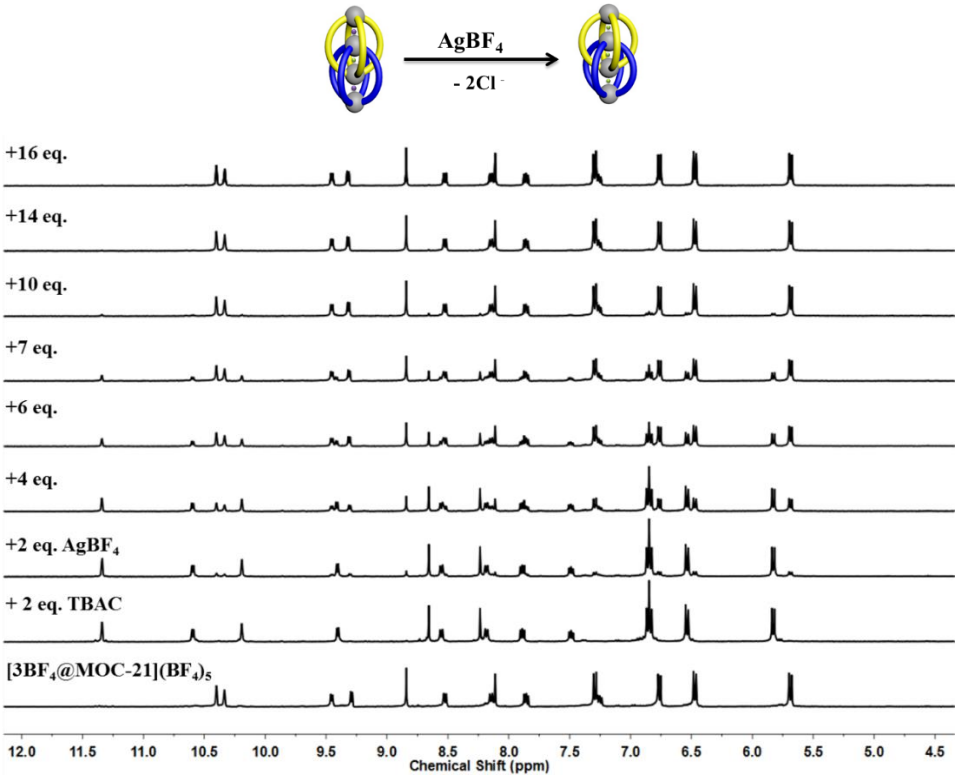

Figure S50. Titration of $AgBF_4$ to the solution of **[2Cl+BF$_4$@MOC-21]$^{5+}$** (400 MHz, CD_3CN, 298 K). **[3BF$_4$@MOC-21](BF$_4$)$_5$** was regenerated quantitatively after adding 16 equiv. of Ag^+.

6.2 Binding affinity for Br^- over BF_4^- with the interlocked cage

Similarly, the NMR titration of **[2Br+BF$_4$@MOC-21](BF$_4$)$_5$** by $AgBF_4$ was applied to determine the binding constants for bromide over tetrafluoroborate guests by the dimeric interlocked cage. During the titration, the intermediate **[2Br+BF$_4$@MOC-21](BF$_4$)$_5$** is observed but exist only in very small portion, so we calculated the apparent binding constant

K_a^{Br/BF_4} by assuming that there are only H and HG_2 in this case. We derived the middle point of the titration to be 1.2 equiv. (1.46 μL) of $AgBF_4$ via interpolation method. The change of the concentration (0.66 mM) of **[2Br+BF$_4$@MOC-21](BF$_4$)$_5$** can be ignored.

In this case, $[Ag^+]$ and $[BF_4^-]$ was calculated:

$$[Ag^+] = (1.2 - 1) \cdot 0.66 \text{ mM} = 0.13 \text{ mM} \quad \text{(S5)}$$

$$[BF_4^-] = (1.2 + 7 - 2 \cdot 0.5) \cdot 0.66 \text{ mM} = 4.75 \text{ mM} \quad \text{(S6)}$$

Using the method above, we could obtain the K_a and ΔG_{ex} for Br^- as:

$$K_a^{Br/BF_4} = 9.6\times10^{13}, \quad \Delta G_{ex}^{Br/BF_4} = -79.8 \text{ kJ mol}^{-1}$$

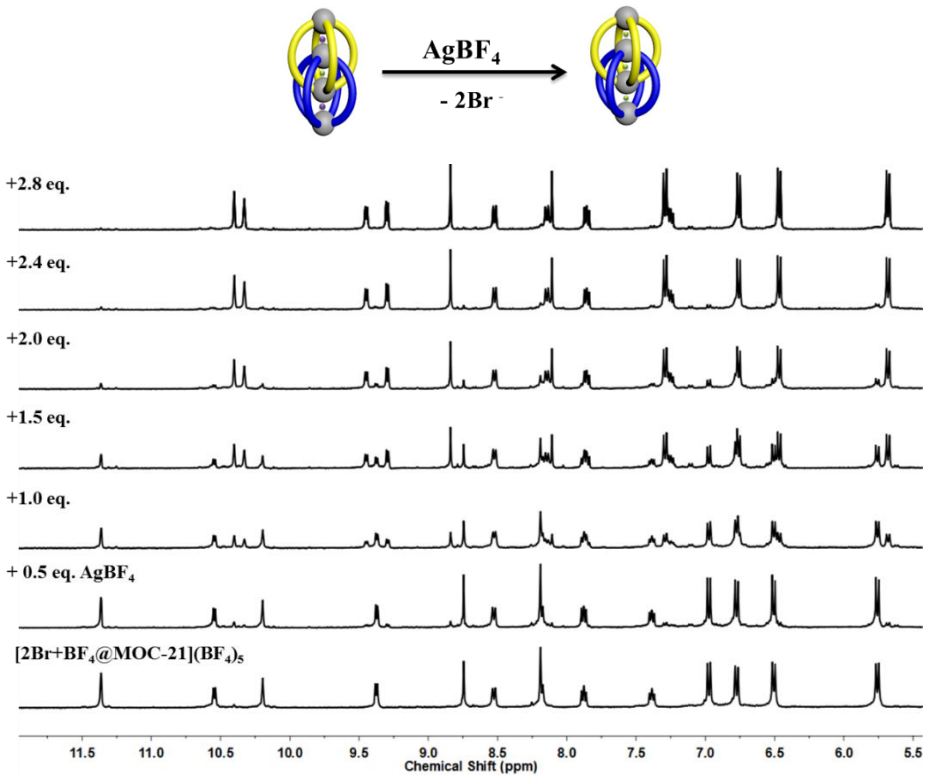

Figure S51. Titration of $AgBF_4$ to the solution of **[2Br+BF$_4$@MOC-21]$^{5+}$** (400 MHz, CD_3CN, 298 K). **[3BF$_4$@MOC-21](BF$_4$)$_5$** was regenerated quantitatively by adding 2.8 equiv. of Ag^+.

6.3 Binding affinity for I^- over BF_4^- with the interlocked cage

Determining binding constant of iodide for **[3BF$_4$@MOC-21](BF$_4$)$_5$** is difficult since two equivalent of Ag^+ ions will quantitatively precipitate I^-. Therefore, we introduce another insoluble metal halide solid to estimate a lower limit for binding constant of I^-. Firstly we prepare a 0.36 mM acetone-d_6/CD_3CN(1:1, v/v) solution of **[3BF$_4$@MOC-21](BF$_4$)$_5$**, then we added excessive lead iodide to this solution. The **[2I+BF$_4$@MOC-21]$^{5+}$** gradually formed at room temperature over few days. Finally the host-guest complex would reach the equilibrium with **[3BF$_4$@MOC-21](BF$_4$)$_5$** until the NMR peaks remain unchanged. Integration of the peaks corresponding to the HG_2 and H in combination with the solubility of PbI_2 would help to solve

the binding constant of iodide.

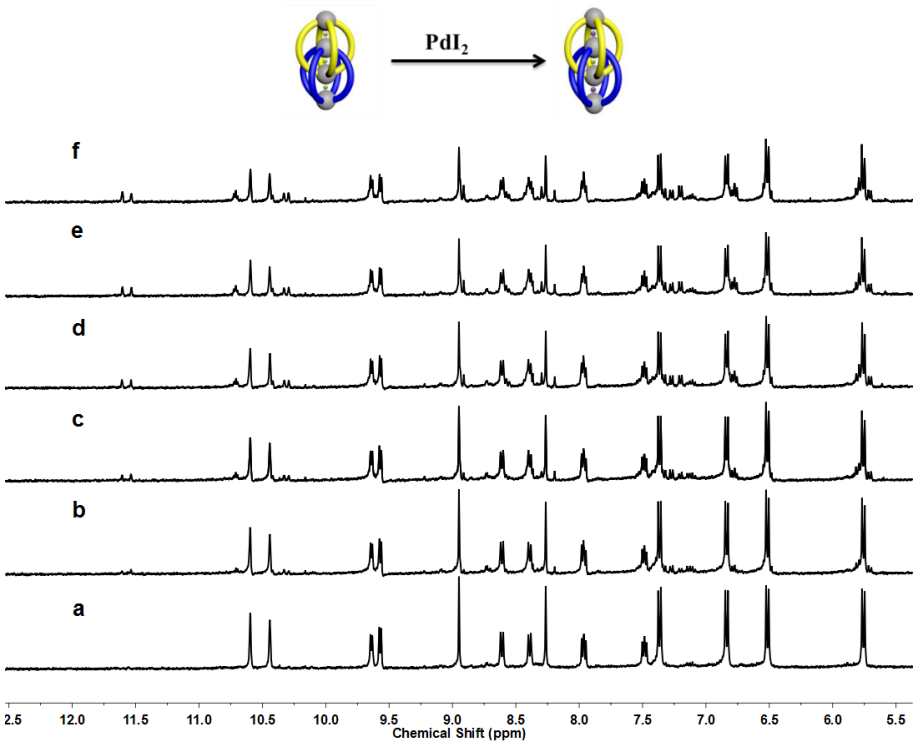

Figure S52. ^{1}H NMR spectra of (a) **[3BF$_4$@MOC-21](BF$_4$)$_5$** before adding PdI_2, (b) 19 h, (c) 29 h, (d) 42 h, (e) 52 h, and (f) 65 h after adding PdI_2 in acetone-d_6/CD_3CN (1:1, v/v) (400 MHz, 298 K).

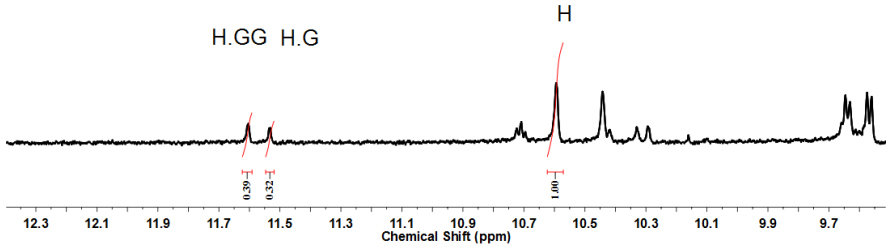

Figure S53. Integration of the peaks for **[3BF$_4$@MOC-21](BF$_4$)$_5$**–H, **[I+2BF$_4$@MOC-21]$^{5+}$**–HG and **[2I+BF$_4$@MOC-21]$^{5+}$**–HG_2 from above spectrum (f) in Figure S53.

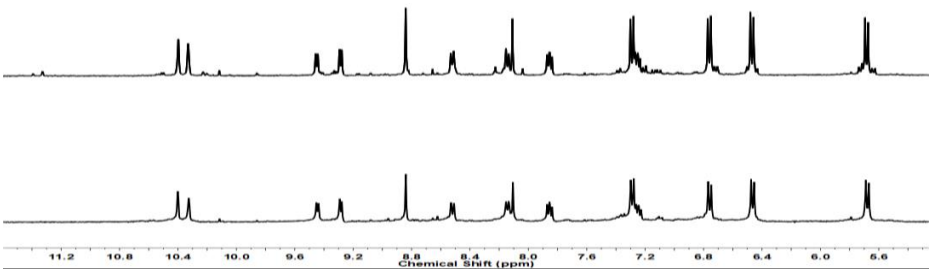

Figure S54. Bottom: ^{1}H NMR spectrum of **[3BF$_4$@MOC-21](BF$_4$)$_5$**, Top: spectrum after three days by adding excessive lead iodide (CD_3CN, 400 MHz, 298 K). Formation of relatively smaller amount of the host-guest complex in pure CD_3CN solution in comparison to that in acetone-d_6/CD_3CN mixed solution (Figure S54) indicates a lower solubility of PdI_2 in pure acetonitrile.

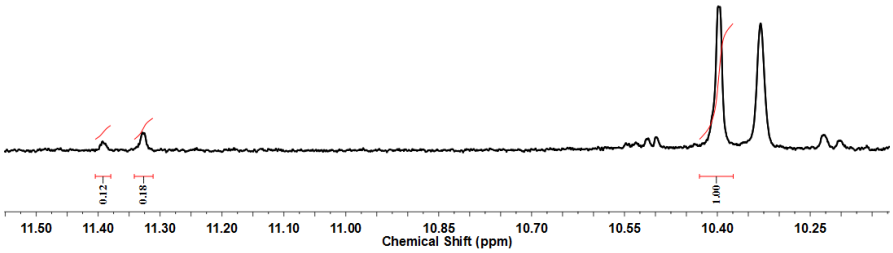

Figure S55. Integration of the peaks for **[3BF$_4$@MOC-21](BF$_4$)$_5$**–H, **[I+2BF$_4$@MOC-21]$^{5+}$**–HG and **[2I+BF$_4$@MOC-21]$^{5+}$**–HG$_2$ from above top spectrum in Figure S54.

The equation for the K_a of I^- is an analogue to S1:

$$K_a^{I/BF_4} = \frac{[\mathbf{2I+BF_4@MOC-21}]\cdot[BF_4^-]^2}{[\mathbf{3BF_4@MOC-21}]\cdot[I^-]^2} \qquad \text{(S7)}$$

Now we need to calculate the concentration of I^- and BF_4^- to calculate the K_a of iodide. The K_{sp} ($\approx 10^{-18.55}$) of PbI_2 is only available for the acetone solvent.[8] However, because of the poor solubility of the host-guest complex in acetone, we chose a mixed solution of acetone-d_6/CD_3CN (1:1, v/v) to estimate the binding constant. We believe the PbI_2 has lower solubility in acetonitrile than in acetone because less host-guest complex is formed in acetonitrile than in a mixed solution of acetone-d_6/CD_3CN (Figures S54-55). So the K_a we calculate here represents a lower boundary for iodide guest:

$$K_a^{I/BF_4} = 0.39 \times \frac{[BF_4^-]^2}{[I^-]^2} \qquad \text{(S8)}$$

$$[BF_4^-] = (8 - 3 \times \frac{1}{(1+0.39+0.32)} - 2 \times \frac{0.32}{(1+0.39+0.32)} - \frac{0.39}{(1+0.39+0.32)}) \cdot 0.36\ \text{mM} = 2.04\ \text{mM} \qquad \text{(S9)}$$

$$[I^-] < \sqrt{K_{sp}^{PbI_2}/Pb^{2+}} = \sqrt{10^{-18.55} \div ((0.32 \div 2 + 0.39) \div (1 + 0.39 + 0.32)) \times 0.36} = 4.92 \times 10^{-8}\ \text{M} \qquad \text{(S10)}$$

Combining S8, S9 and S10, lower boundary of K_a^{I/BF_4} and ΔG_{ex} could be derived as:

$$K_a^{I/BF_4} > 6.7 \times 10^8, \quad \Delta G_{ex}^{I\,/\,BF_4} < -50.4\ \text{kJ mol}^{-1}$$

6.4 Binding affinity for NO_3^- over BF_4^- with the interlocked cage

According to above anion exchange study, replacing of BF_4^- guest from the interlocked cage **[3BF$_4$@MOC-21](BF$_4$)$_5$** by in NO_3^- proceeds completely to exchange all three BF_4^- guests. The exchange is a slow and equilibrium reaction. Therefore, the anion affinity of the interlocked cage for NO_3^- guests over **BF_4^-** can be estimated by using the Hill function to measure the apparent association constant K_a.[9] As seen from Figure S43, in CD_3CN solution the following anion exchange reaction

$$\mathbf{[3BF_4@MOC\text{-}21]^{5+} + 3NO_3^- \rightarrow [3NO_3@MOC\text{-}21]^{5+} + 3BF_4^-}$$

can be considered to proceed through formation of three host-guest species of HG-**[NO$_3$+2BF$_4$@MOC-21]$^{5+}$**, HG$_2$-**[2NO$_3$+BF$_4$@MOC-21]$^{5+}$** and HG$_3$-**[3NO$_3$@MOC-21]$^{5+}$**,

which was detected clearly by the ^{1}H NMR spectra. Through integration of the corresponding proton peaks and conversion into the concentration of the host-guest species, we could obtain the constant K_a via fitting the Hill equation using linear regression analysis.

Based the NMR spectra of Figures S43, The data from titration could be fit to a traditional linear model according to the Hill equation[10]

$$\log\frac{\theta}{1-\theta} = n\log[G] + \log\ K_a$$

where θ is saturated ratio which stands for the fraction of binding sites occupied by the guest, $[G]$ is the guest concentration, n is the Hill coefficient describing cooperativity, and K_a is the apparent association constant. We obtained the relative abundances of the different species during the titration after integration. Therefore, the apparent binding constant and Gibbs free energy could be obtained as:

$$K_a^{NO_3^-/BF_4^-} = 10^{9.66} = 4.6\times10^9,\quad \Delta G_{ex}^{NO_3^-/BF_4^-} = \text{-}55.1\ \text{kJ mol}^{-1}$$

Table S9. Relative abundances of the different species[a] and calculation of the saturated ratio θ after addition of TBAN.

H	HG	HG_2	HG_3	H_t	θ	$\theta/(1-\theta)$	$\lg\theta/(1-\theta)$
0.93	0.07	1	0	2.08	0.331731	0.496403	-0.30417
0	0.24	0.94	0.93	2.11	0.775671	3.457746	0.538793
0	0	0.2	1	1.22	0.939891	15.63636	1.194136

[a] HG_n represents abundance of host-guest complex between **MOC-21** and NO_3^-, H_t is total host abundance whereas H stands for free host abundance.

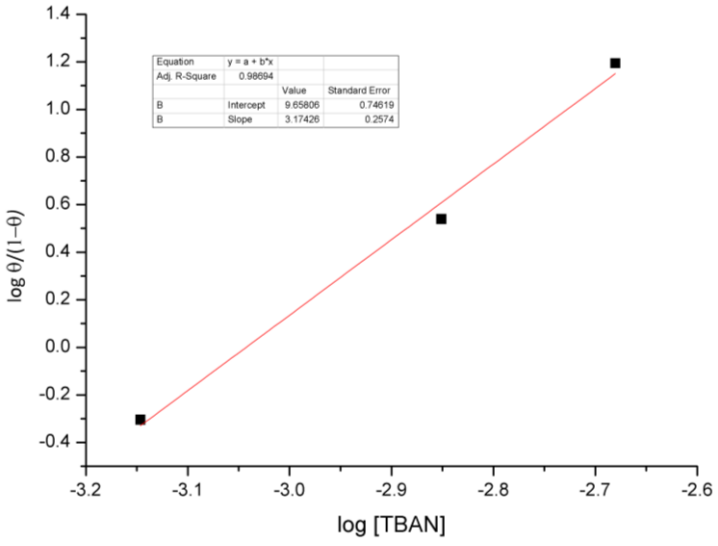

Figure S56. Hill function θ vs. lg[TBAN] in CD_3CN solution. (θ represents the fraction of HG-**[NO_3+2BF_4@MOC-21]$^{5+}$**, HG_2-**[2NO_3+BF_4@MOC-21]$^{5+}$** and HG_3-**[3NO_3@MOC-21]$^{5+}$** species) with respect to free guest concentration (equal to TBAN added) at 298 K.

7. Spontaneous monomerization and dimerization upon suitable template

7.1 Kinetics for degradation of cage [MOC-21](BF$_4$)$_8$ in DMSO

Degradation process was studied by ^{1}H NMR technique using DMSO-d_6 as the solvent. Around 1.5 mg **[MOC-21](BF$_4$)$_8$** was added to a NMR tube, dissolved by 0.4 mL DMSO-d_6. ^{1}H NMR spectra were recorded periodically afterwards.

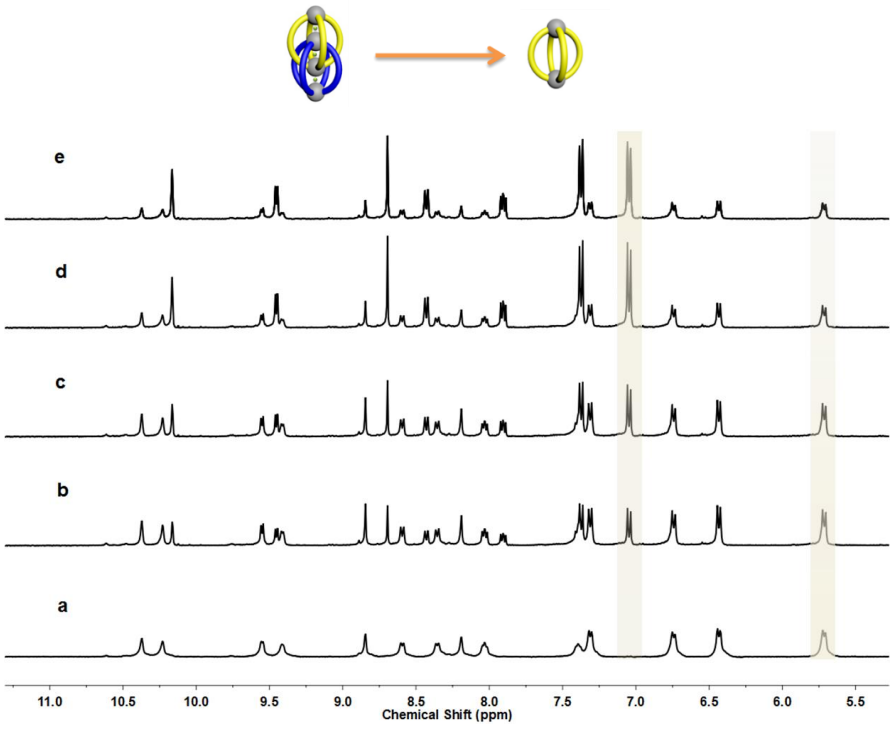

Figure S57. a) ^{1}H NMR spectra of **[3BF$_4$@MOC-21](BF$_4$)$_5$** (0.90 mM) in DMSO-d_6 at 298 K for b) 781 min, c) 1166 min, d) 2242 min, e) 2703 min. Peaks (H_g from **[MOC-20](BF$_4$)$_4$** and $H_{g'}$ from **[3BF$_4$@MOC-21](BF$_4$)$_5$**) highlighted were integrated to calculate the molar ratio of the dimer. Peaks from **[MOC-20](BF$_4$)$_4$** disappeared completely after one week, indicating complete structural conversion.

The fraction of **[3BF$_4$@MOC-21](BF$_4$)$_5$** was plotted as a function of time and fitted assuming first-order kinetics to an exponential decay function. Furthermore, the concentration of the dimer with respect to reaction time was fitted to the integrated first order rate law to yield a rate constant.

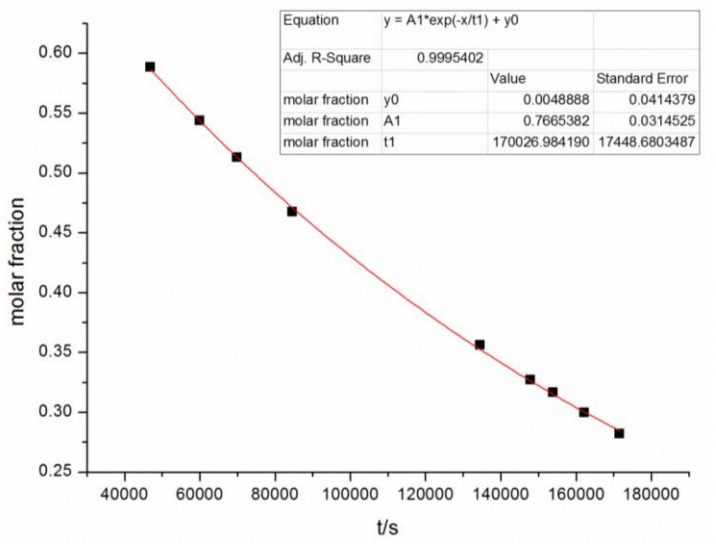

Figure S58. Molar fraction of **[3BF$_4$@MOC-21](BF$_4$)$_5$** plotted versus time at 298 K based on integration of the ^{1}H NMR peaks, indicating a first-order transformation from dimer to monomer.

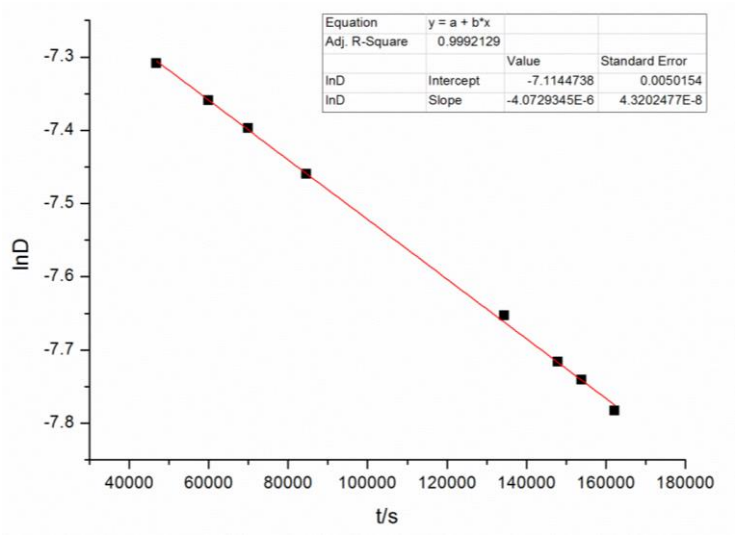

Figure S59. Linear plot of ln[**[3BF$_4$@MOC-21](BF$_4$)$_5$**] (D represents dimer concentration of **[3BF$_4$@MOC-21](BF$_4$)$_5$**) with respect to reaction time at 298 K , from which a rate constant of $(4.07 \pm 0.04) \times 10^{-6}$ s^{-1} was obtained.

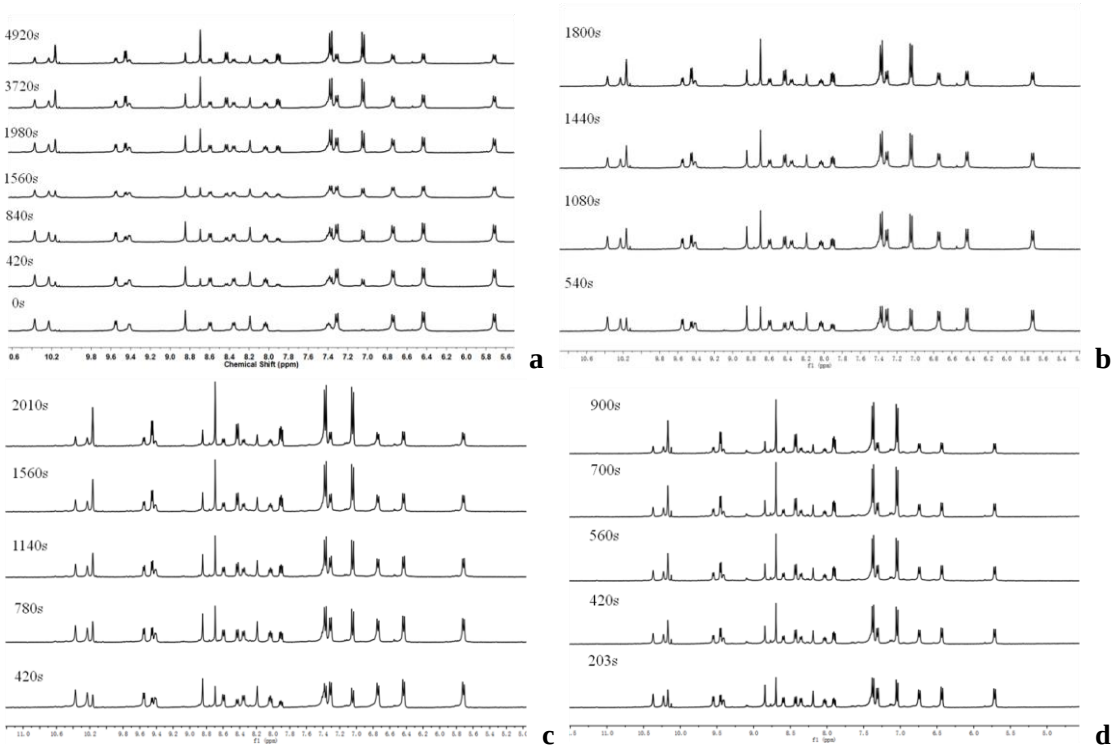

Figure S60. ^{1}H NMR spectra of **[3BF$_4$@MOC-21](BF$_4$)$_5$** (0.90 mM) in DMSO-d_6 at 323 K a), 333 K b), 343 K c) and 353 K d).

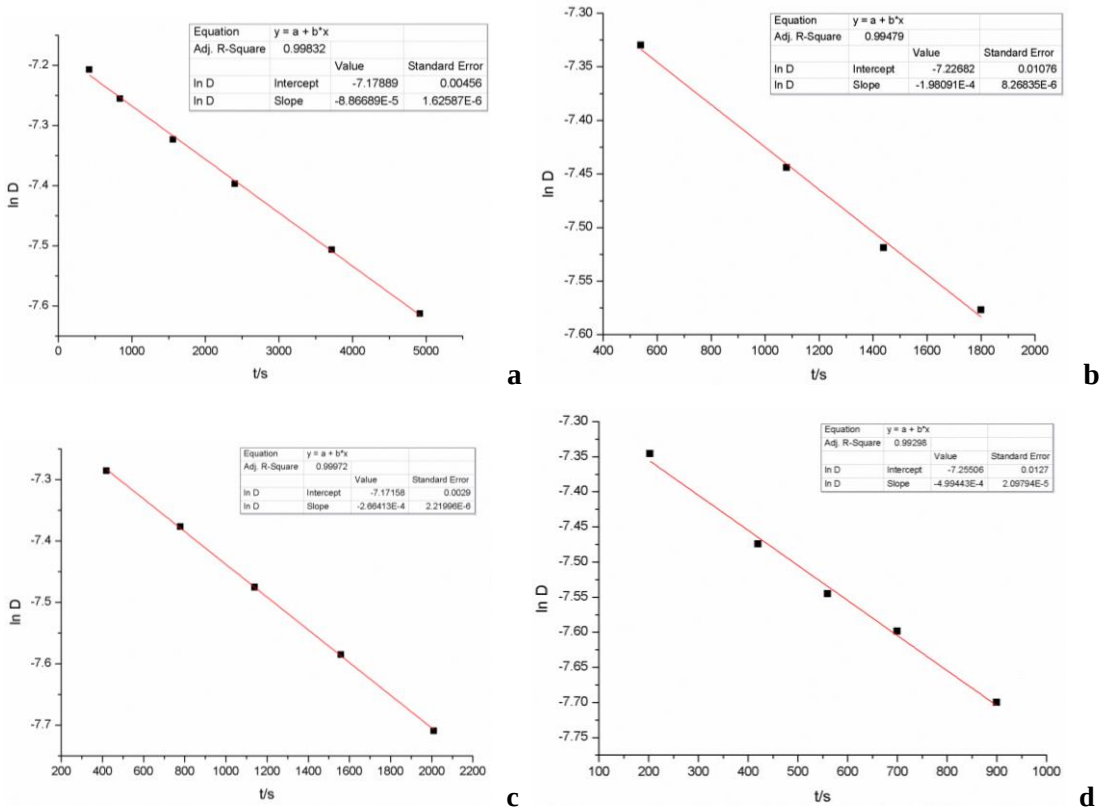

Figure S61. Linear plots of ln[**[3BF$_4$@MOC-21](BF$_4$)$_5$**] (D represents dimer concentration of **[3BF$_4$@MOC-21](BF$_4$)$_5$**) with respect to reaction time at 323 K a), 333 K b), 343 K c and 353 K d).

Table S10. Summary of the calculated kinetic data of degradation process.

T/K	k/ s^{-1}	k/T	1/T	lnk/T
298	4.07×10^{-6}	1.37×10^{-8}	0.003356	-18.1082
323	8.87×10^{-5}	2.75×10^{-7}	0.003096	-15.1083
333	1.98×10^{-4}	5.95×10^{-7}	0.003003	-14.3349
343	2.66×10^{-4}	7.77×10^{-7}	0.002915	-14.0682
353	4.99×10^{-4}	1.41×10^{-6}	0.002833	-13.4685

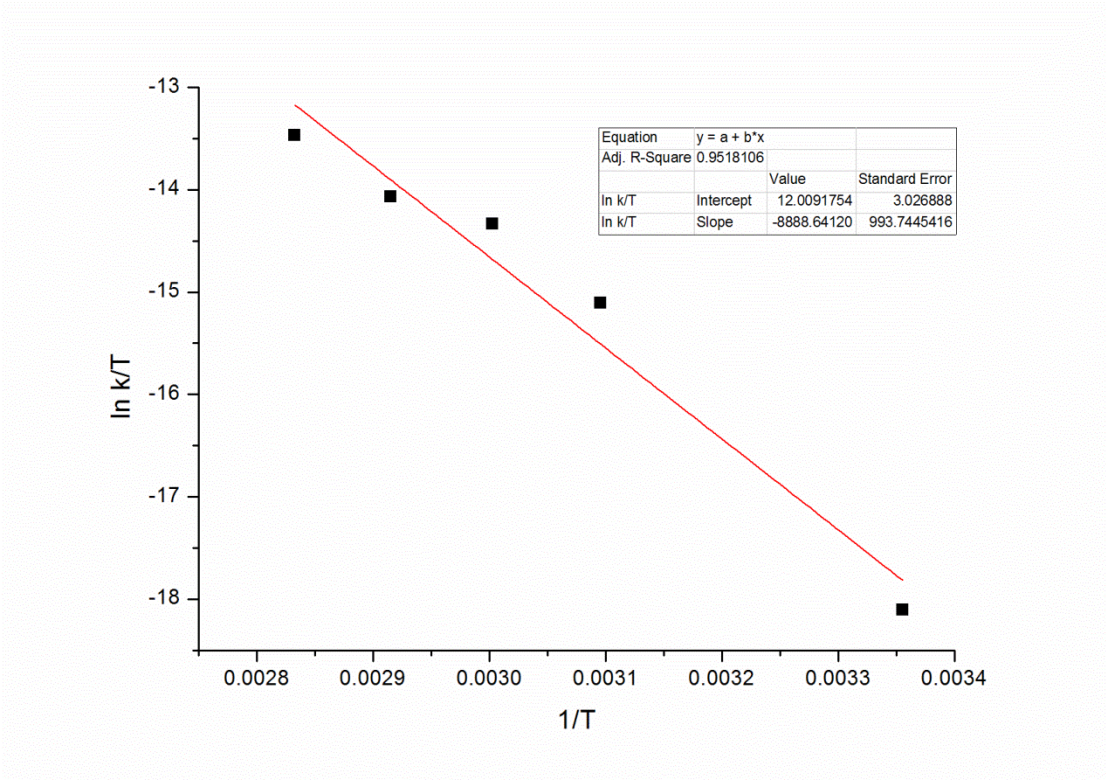

Figure S62. Eyring plot to yield the activation parameters over temperature 323-353 K.

According to equation: $\ln\frac{k}{T} = \frac{-\Delta H_a}{R}\times\frac{1}{T} + \ln\frac{k_B}{h} + \frac{\Delta S_a}{R}$

$\Delta H_a^{BF_4}$ = 73.9 ± 8.3 kJ mol^{-1}

$\Delta S_a^{BF_4}$ = - 97.7 ± 25.2 J mol^{-1} K^{-1}

For 298 K, $\Delta E_a^{BF_4} = \Delta H_a^{BF_4} - T\Delta S_a^{BF_4}$ = 103.0 kJ mol^{-1}

7.2 Kinetics for dimerization of cage [MOC-20](NO$_3$)$_4$ in DMSO

Different form monomerization simply from one interlocked species, dimerization reaction involves at least two monomers, and probably encapsulation of NO_3^- anions. To simplifying the process treatment, excess NO_3^- anions are added to reach a saturated solution, thereof minimizing the influence of NO_3^- anions on the reaction. A 50 μL DMSO-d_6 solution of the ligand (74 mM) and ca. 7 equiv. $TBANO_3$ was added to the NMR tube, then 400 μL pure DMSO-d_6 was added to dilute the ligand solution. 10 μL DMSO-d_6 solution of $Pd(NO_3)_2$ (148 mM) was then added to the tube. NMR tube was shaken for 5 minutes before left to the oil bath under corresponding temperature.

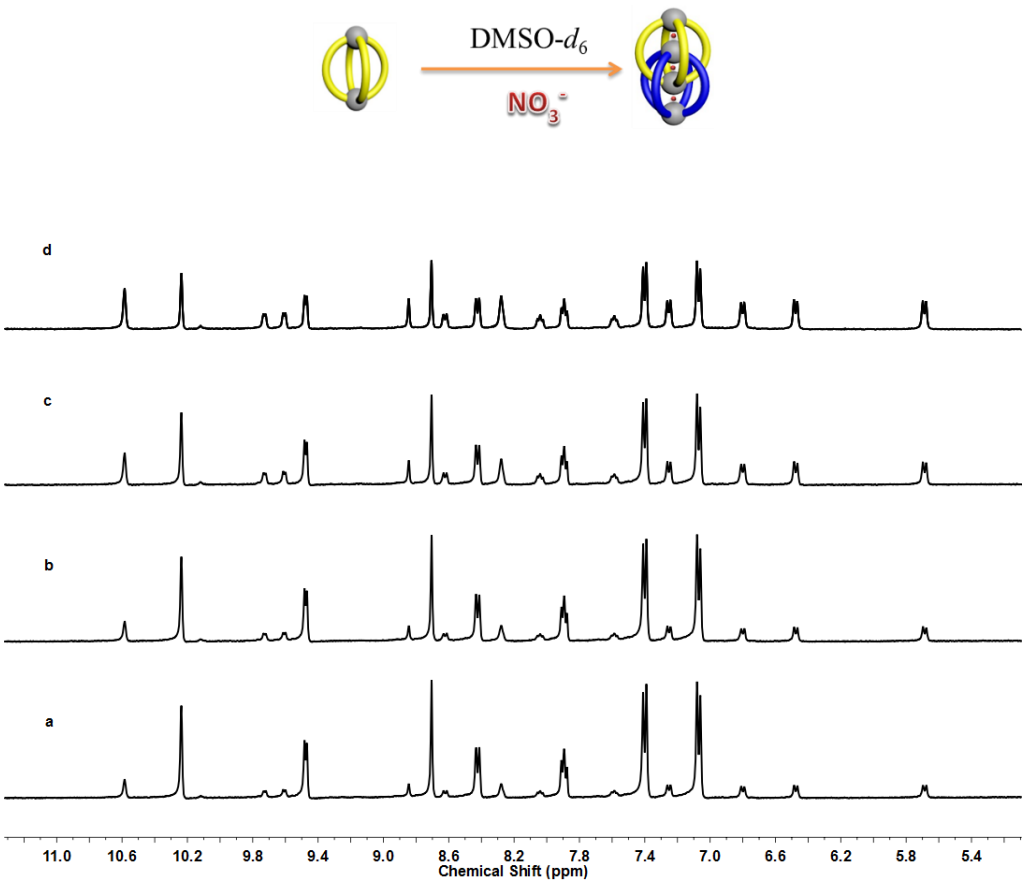

Figure S63. ^{1}H NMR of the **[MOC-20](NO$_3$)$_4$** (2.01 mM) in DMSO-d_6, after heating in a 308 K oil bath for a) 70800s, b) 85200s , c) 154800s, d) 255600s. The reciprocal of concentration of the monomer with respect to reaction time was fitted to the integrated second order rate law to yield a rate constant.

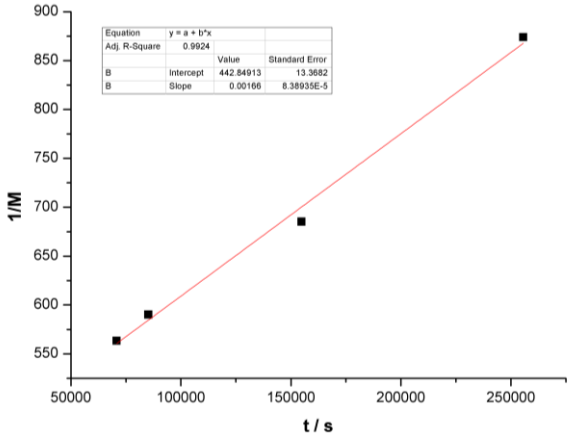

Figure S64. Linear plot of 1/M (M represents the monomer concentration of **[MOC-20](NO$_3$)$_4$**) with respect to reaction time at 308 K.

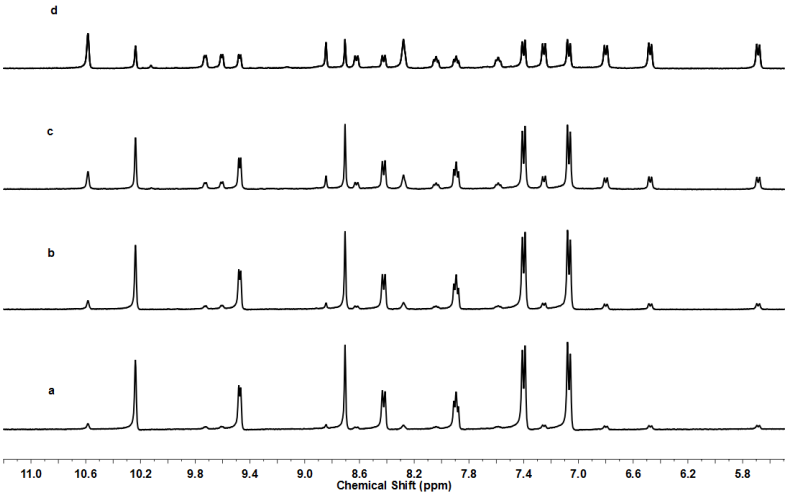

Figure S65. ^{1}H NMR of the **[MOC-20](NO$_3$)$_4$** (2.01 mM) in DMSO-d_6, after heating in a 318 K oil bath for a) 6733s, b) 11280s , c) 26940s, d) 79890s. The reciprocal of concentration of the monomer with respect to reaction time was fitted to the integrated second order rate law to yield a rate constant.

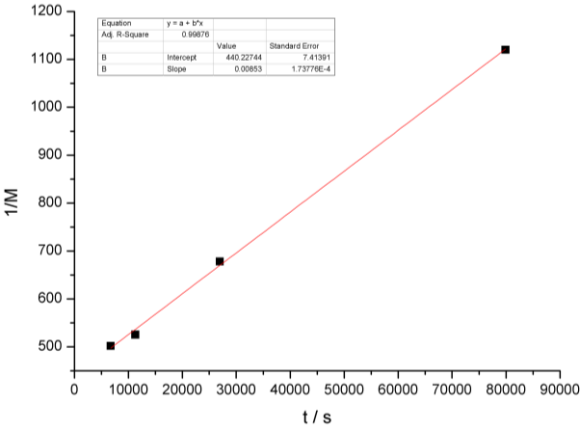

Figure S66. Linear plot of 1/M (M represents the monomer concentration of **[MOC-20](NO$_3$)$_4$**) with respect to reaction time at 318 K.

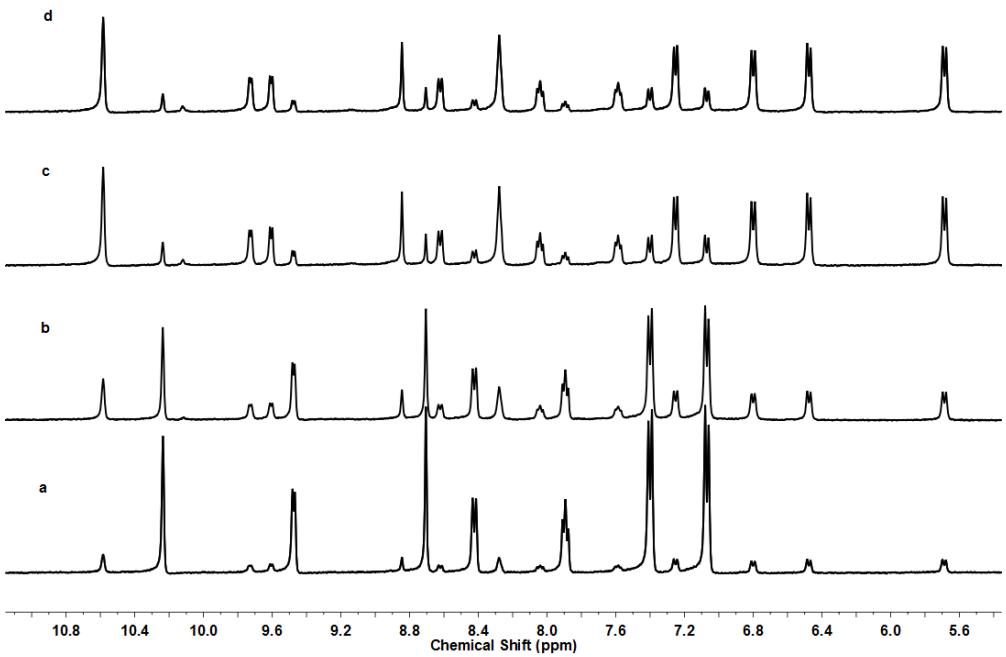

Figure S67. ^{1}H NMR of the **[MOC-20](NO$_3$)$_4$** (2.01 mM) in DMSO-d_6, after heating in a 328 K oil bath for a) 2035s, b) 7440s , c) 69600s, d) 84000s. The reciprocal of concentration of the monomer with respect to reaction time was fitted to the integrated second order rate law to yield a rate constant.

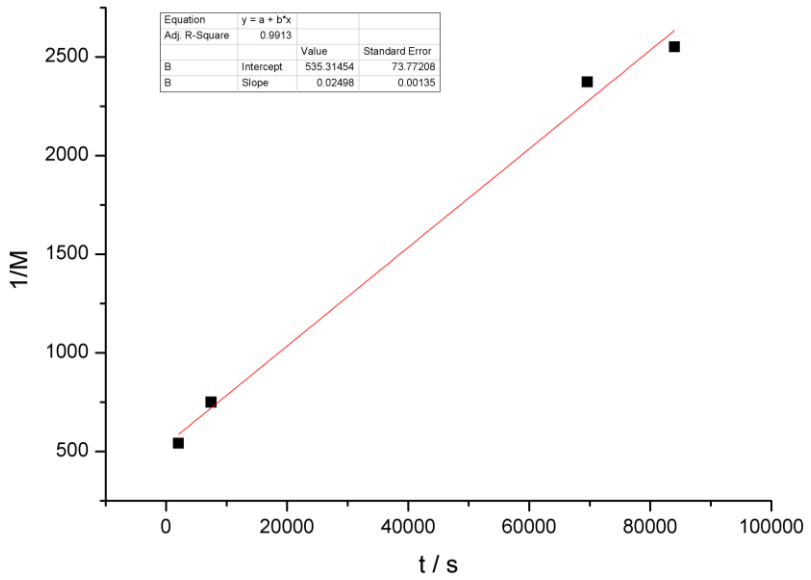

Figure S68. Linear plot of 1/M (M represents the monomer concentration of **[MOC-20](NO$_3$)$_4$**) with respect to reaction time at 328 K.

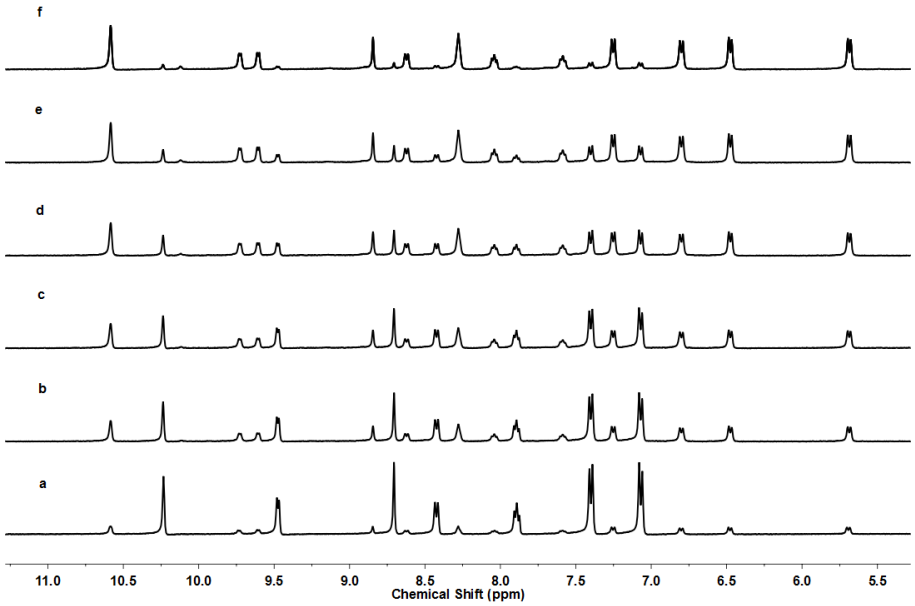

Figure S69. ^{1}H NMR of the **[MOC-20](NO$_3$)$_4$** (2.01 mM) in DMSO-d_6, after heating in a 338 K oil bath for a) 1470s, b) 3930s , c) 5520s, d) 10003s, e) 16860s and f) 68400s. The reciprocal of concentration of the monomer with respect to reaction time was fitted to the integrated second order rate law to yield a rate constant.

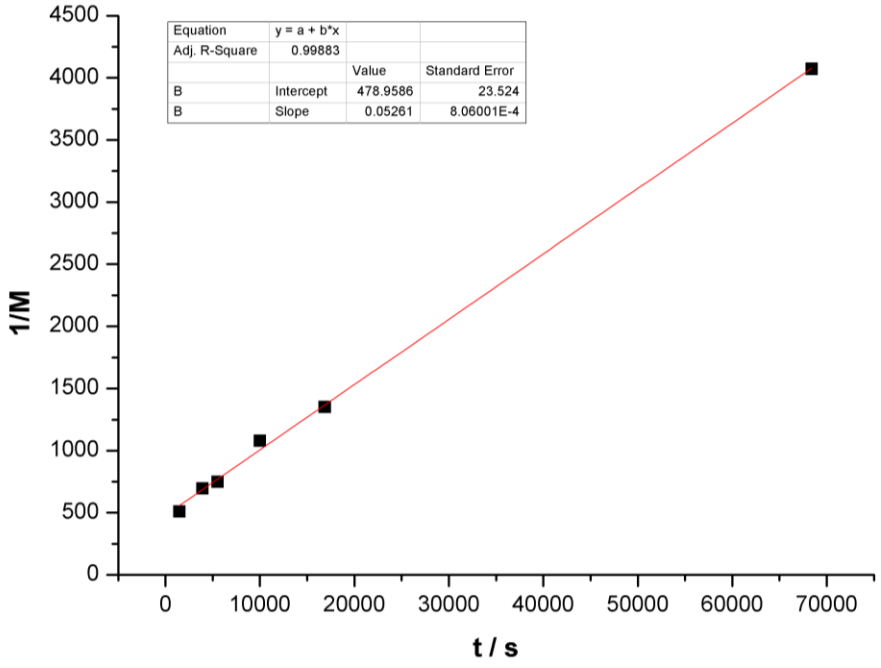

Figure S70. Linear plot of 1/M (M represents the monomer concentration of **[MOC-20](NO$_3$)$_4$**) with respect to reaction time at 338 K.

Table S11. Summary of the calculated kinetic data of dimerization process of [**MOC-20](NO$_3$)$_4$** in the presence of nitrate template.

T/K	k/M^{-1}·s^{-1}	k/T	1/T	lnk/T
318	0.00166	5.38961×10^{-6}	0.003247	-12.131
328	0.00853	2.68239×10^{-5}	0.003145	-10.5262
338	0.02498	7.61585×10^{-5}	0.003049	-9.48269
348	0.05261	1.57515×10^{-4}	0.002994	-8.75599

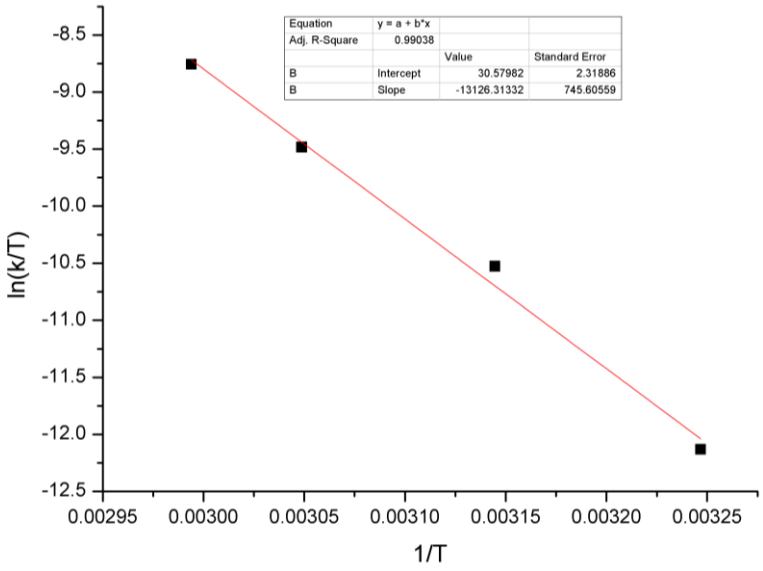

Figure S71. Eyring plot to yield the activation parameters over temperature 308-338 K.

$$\Delta H_a^{NO_3} = 109.3 \pm 6.2 \text{ kJ mol}^{-1}$$

$$\Delta S_a^{NO_3} = 56.7 \pm 19.3 \text{ J mol}^{-1} \text{ K}^{-1}$$

For 318 K, $\Delta E_a^{NO_3} = \Delta H_a^{NO_3} - T\,\Delta S_a^{NO_3} = 91.3 \text{ kJ mol}^{-1}$

7.3 Thermodynamics for dimerization of cage [MOC-20](NO$_3$)$_4$ in DMSO

Dimerization of the monomeric **[MOC-20](NO$_3$)$_4$** to the interlocked **[3NO$_3$@MOC-21](NO$_3$)$_5$** is not a complete reaction because the ^{1}H NMR spectral study indicates that there is an equilibrium between the monomer and dimer during the structural conversion, and the final state remains unchanged for several days. Therefore, if we take the final state of the reactions at above four temperatures, we are able to estimate the thermodynamics of the dimerization process by applying the Van't Hoff equation with linear regression analysis.[11] It should be noted that this is only an approximate estimation without consideration of the exact state of anions.

Table S14. Summary of the calculated thermodynamic data of dimerization process of [**MOC-20](NO$_3$)$_4$** in the presence of nitrate template.

T/K	K_{eq}	ln K_{eq}
308	1.09×10^3	6.99
318	3.55×10^3	8.18
328	6.77×10^3	8.82
338	1.59×10^4	9.67

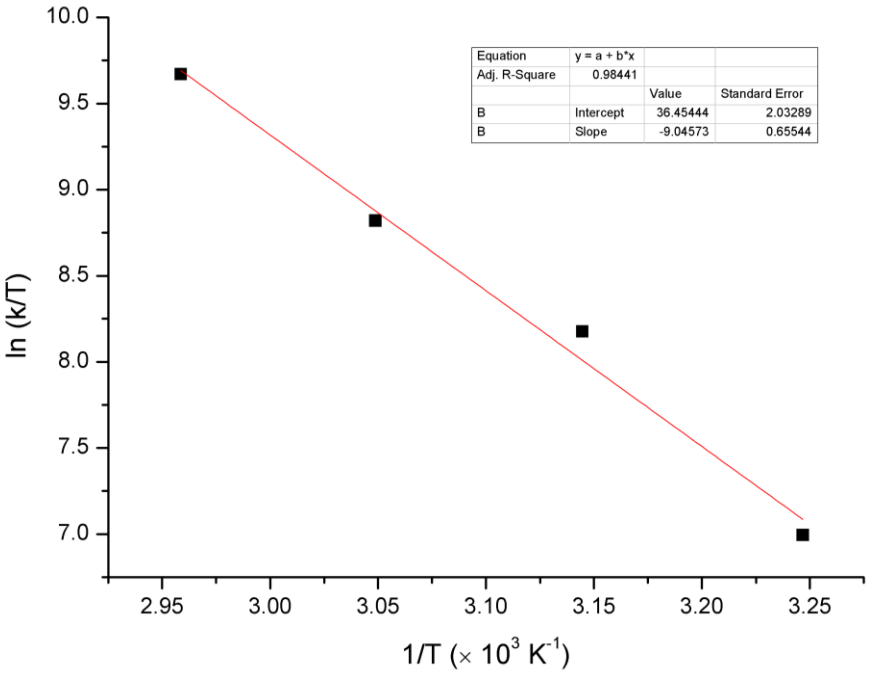

Figure S72. Van't Hoff plot after equilibrium over temperature 318-348 K to yield thermodynamic parameters.

According to Van't Hoff equation: $\ln K_{eq} = \frac{-\Delta H}{RT} + \frac{\Delta S}{R}$

$$\Delta H^{NO_3} = 75.2 \pm 5.5 \text{ kJ mol}^{-1}$$

$$\Delta S^{NO_3} = 303.1 \pm 16.9 \text{ J mol}^{-1} \text{ K}^{-1}$$

For 318 K, the apparent free energy is estimated as:

$$\Delta G^{NO_3} = \Delta H^{NO} - T\Delta S^{NO_3} = -18.1 \text{ kJ mol}^{-1}$$

8. Dimerization induced by cisplatin

[MOC-20](BF$_4$)$_4$ was dissolved in DMSO-d_6, then this solution was diluted by large amount of CD_3CN. ^{1}H NMR spectra were recorded after addition of ca. two eq cisplatin (normally below 0.5 mg) at certain points. The amine of cisplatin could be observed clearer by tuning down the ratio of DMSO-d_6/CD_3CN since cisplatin is well soluble in DMSO. ESI–MS spectrum was also recorded after the transformation to identify the product and newly formed platinum complex. Noticeably, this complete dimerization

proceeds for two days in the presence of ca. 2 eq. of cisplatin (CD_3CN/DMSO-d_6 = 7:1, v/v), imitating a similar solvation reaction of cisplatin inside the cell through formation of $[PtCl(DMSO)(NH_3)_2]^+$ and slow release of Cl^-.

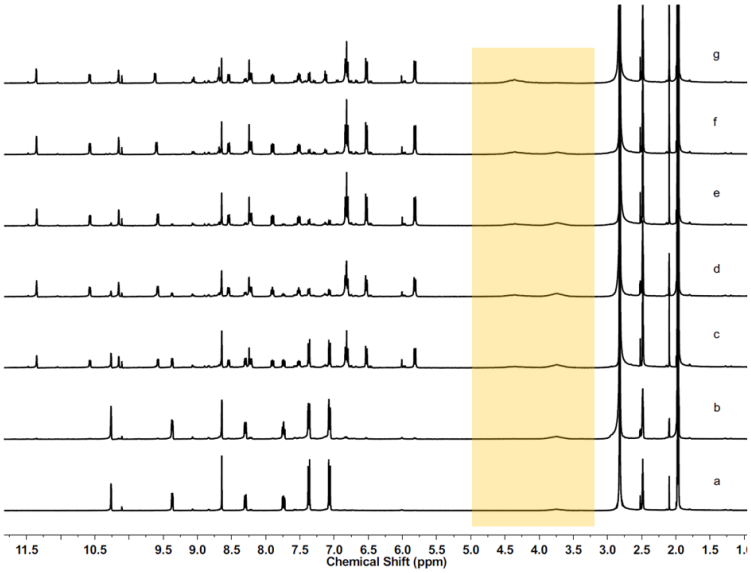

Figure S73. Monomer **[MOC-20](BF$_4$)$_4$** was dimerized in presence of cisplatin in DMSO-d_6/CD_3CN (1:4.67, v/v, 400 MHz, 298 K): ^{1}H NMR spectra recorded in (a) 0 min; (b) 42 min; (c) 249 min; (d) 328 min; (e) 373 min; (f) 594 min and (g) 1401 min after adding the cisplatin. Peaks highlighted in yellow shift downfield during the process, showing influence of coordination change to the protons of ammonia in cisplatin.

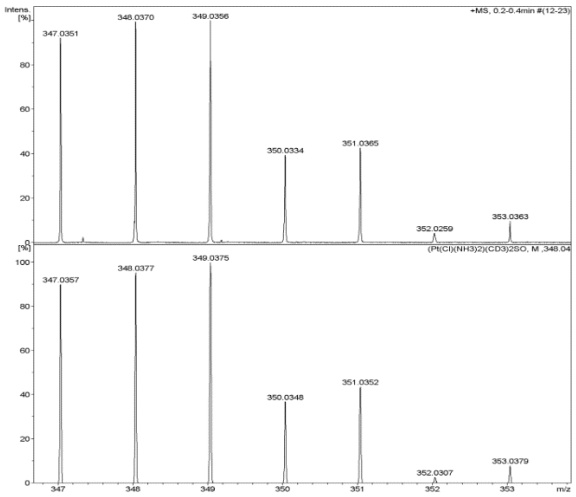

Figure S74. The sample was diluted with acetonitrile and subject to high resolution ESI-mass spectrometry after the dimerization. Theoretical isotope pattern (bottom) of the assumed complex $[PtNH_3(CD_3)_2SO]Cl^+$ matches well with the highest peak observed (top) on the mass spectrum.

References

(1) Wang, Q.; Yang, R.; Zhuang, C.-F.; Zhang, J.-Y.; Kang, B.-S.; Su, C.-Y. Eur. J.

Inorg. Chem. 2008, 2008, 1702

(2) R. Sekiya, M. Fukuda and R. Kuroda, *J. Am. Chem. Soc.*, 2012, **134**, 10987-10997.

(3) H. Lee, P. Elumalai, N. Singh, H. Kim, S. U. Lee and K.-W. Chi, *J. Am. Chem. Soc.*, 2015, **137**, 4674-4677.

(4) A) Kleywegt, G. J.; Jones, T. A. Detection, delineation, measurement and display of cavities in macromolecular structures. Acta. Cryst. D50, 1994, 178; b) S. Mecozzi and J. J. Rebek, *Chem.-Eur. J.*, 1998, **4**, 1016-1022

(5) Clegg, J. K.; Cremers, J.; Hogben, A. J.; Breiner, B.; Smulders, M. M. J.; Thoburn, J. D.; Nitschke, J. R. Chem. Sci. 2013, 4, 68.

(6) Freye, S.; Engelhard, D. M.; John, M.; Clever, G. H. Chem.-Eur. J. 2013, 19, 2114.

(7) Luehrs, D. C.; Iwamoto, R. T.; Kleinberg, J. Inorg. Chem. 1966, 5, 201.

(8) Ramadan, A. A.; Mandil, H.; Anadani, L. Int. J. Pharm. Pharm. Sci. 6, 203.

(9) Connors, K. A. Binding Constants: The Measurement of Molecular Complex Stability; Wiley: New York, 1987.

(10) Hill, A. V. Biochem. J. 1913, 7, 471

(11) Gan, Q.; Ronson, T. K.; Vosburg, D. A.; Thoburn, J. D.; Nitschke, J. R. *J Am Chem Soc* **2015**, *137*, 1770.